Theses and Dissertations

2004

# Microstructural investigation of metal-oxide supported gold and gold alloy catalysts

Andrew A. Herzing
*Lehigh University*

Follow this and additional works at: http://preserve.lehigh.edu/etd

### Recommended Citation

# Herzing, Andrew A.

# Microstructural Investigation of Metal-Oxide Supported Gold and Gold Alloy Catalysts

# September 2004

# Microstructural Investigation of Metal-Oxide Supported Gold and Gold Alloy Catalysts

by

Andrew A. Herzing

A Thesis
Presented to the Graduate and Research Committee
Of Lehigh University
In Candidacy for the Degree of
Master of Science

In
Materials Science and Engineering

Lehigh University

August 13, 2004

This thesis is accepted and approved in partial fulfillment of the requirements for the Master of Science.

8-10-04

Date

Thesis Advisor

Chairperson of Department

# Acknowledgements

The work detailed in this thesis would not have been possible without the kind assistance of many people. In particular, I would like to thank my adviser Dr. Christopher Kiely for his constant encouragement and for generously giving an enormous amount of his time to keep me on track whenever an obstacle was encountered.

Also, I would like to thank David Ackland for the training and assistance he has given me in operating the instruments in Lehigh University's electron microscopy lab.

Similarly, I owe a great deal to Dr. Masashi Watanabe who assisted me in the art of analytical electron microscopy and performed statistical analysis on many of the images I presented in this thesis.

Also, Dr. Andrew Burrows was kind enough to help with the interpretation and analysis of the lattice images presented within.

Next, I would like to thank Dr. Graham Hutchings and his group at Cardiff University, in particular Drs. Albert Carley and Philip Landon, for synthesizing and testing the catalysts discussed in this thesis.

Finally, Dr. Bruce Gates at the University of California-Davis performed the EXAFS and XANES data presented within.

The very nature of a collaborative project such as this one requires the constant attention and communication of any number of people. I was fortunate enough to have had the opportunity to work with a terrific group of people, some of whom have gone unmentioned on this page but whose help was invaluable to making this a worthwhile endeavor.

# Table of Contents

# List of Tables

# List of Figures

**Abstract:**

Iron oxide supported Au nanoparticles were investigated as catalysts of low-temperature oxidation of CO and they were found to be highly active. This activity was found to be dependent on thermal history and tended to decrease with increasing calcination temperature. This was attributed to the simultaneous reduction of cationic gold species to metallic $Au^0$, an increase in the mean gold particle size, and sintering of the iron oxide support particles. The possible presence of the iron oxy-hydroxide, goethite, was also detected in the high activity catalysts, but not in the catalysts calcined at elevated temperature.

$Au/Fe_2O_3$ catalysts were tested for oxidation of CO in the presence of $H_2$. It was found that selectivity was increased to 100% by calcination at elevated temperature, but this also reduced the CO oxidation activity. 100% selectivity was achieved while retaining a high-level of CO oxidation by calcining at 400 °C for four hours. Electron microscopy was used to determine the structure/property relationship.

Au/Zinc oxide catalysts were investigated for the oxidation of methane. It was found that the lightoff temperature and activation energy for the reaction decreased significantly with increasing gold content up to 2 at.%. The further addition of 5 at.% Au caused the lightoff temperature to increase. A parallel trend was observed in the oxide support particle size, suggesting that the addition of gold stabilized smaller oxide particles and prevented their growth. It is proposed that mono-disperse gold atoms may be responsible for this inhibition as well as being highly active sites for catalysis. The increased support particle size in the sample containing 5 at.% Au may be due to a lack of these highly dispersed gold entities.

Supports consisting of $Al_2O_3$, $TiO_2$, and $Fe_2O_3$ were co-impregnated with gold and palladium for hydrogen peroxide synthesis. It was found for all supports that the catalytic activity was maximized by using a 1:1 Au-Pd ratio. STEM analysis revealed a bi-modal metal particle size distribution of both small and very large particles. While the majority of these were Au-Pd alloys, pure elemental particles of both Au and Pd were also observed. Evidence of surface segregation of Pd was observed, and was due to preferential oxidation of Pd relative to Au during calcination. Discrete NaCl particles were also detected in the haematite supported catalysts.

# Chapter 1 - Introduction and Literature Review

## 1.1 Gold Catalysts – Background

Metals such as platinum, palladium, and rhodium supported on metal-oxides have been used for many years as catalysts for a number of important chemical reactions. In contrast, gold was thought to be chemically inert despite its proximity on the periodic table to the highly catalytically active elements mentioned above. However, in 1989 Haruta et al [1] reported novel catalysts made by co-precipitation from $HAuCl_4$ and the nitrates of various transition metals including iron, cobalt, and nickel. After calcination at 400 °C, the catalysts were found to consist of dispersed Au particles with a mean diameter of 10 nm supported on $\alpha-Fe_2O_3$, $Co_3O_4$, and NiO. These catalysts were shown to be efficient for catalyzing the oxidation of CO (Eq. 1.1) and $H_2$ (Eq 1.2) at low temperature.

$$2CO + O_2 \rightarrow 2CO_2 \qquad (1.1)$$

$$2H_2 + O_2 \rightarrow 2H_2O \qquad (1.2)$$
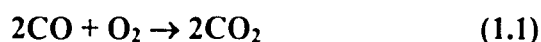
It was reported that this behavior was due to a synergistic effect, since neither gold nor the oxides alone were sufficient to promote the reaction. More impressively, it was found that the catalyst exhibited high activity even at temperatures below 0 °C. This was a striking departure from the high temperatures necessary for catalysis of the same reaction by supported platinum nanoparticles (200 – 250°C).

Since that time, oxide supported gold catalysts were found to be active for many different reactions. These include, but are not limited to, the epoxidation of propylene [2], the water gas shift reaction (WGS) [3], the hydrogenation of unsaturated hydrocarbons [4], and the reduction of nitrogen oxide [5]. In the present discussion,

general observations pertaining to CO oxidation will be considered since the extent of knowledge is much greater for this reaction than any other.

## 1.2 Gold Catalysis – Established Behavior
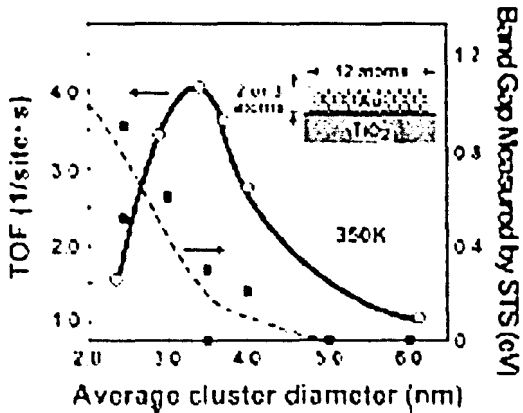
Since the discovery of gold as an oxidation catalyst, a consensus has developed around the various observations reported by researchers throughout the world. First, it is well agreed that the gold particle size plays an important role in the catalytic activity. Research has shown that for gold particles that are larger than 10 nm, very little CO conversion is achieved. As the particles become smaller, the activity increases and exhibits a peak between 3 and 5 nm. Goodman et al. performed an elegant experiment using scanning tunneling microscopy (STM) and electron microscopy to show that there was a correlation between the onset of catalytic activity and changes in the electronic structure of the gold particle at the point where their size reaches 3.5 nm [6]. Illustrated graphically below in Figure 1, the results also showed that the change in electronic structure occurred when the gold clusters were only two atoms in thickness.



Figure 1 - Plot of turn-over-frequency and band-gap measured by STM vs. Au particle diameter [6]

These findings suggest that the catalyst's activity is maximized as one of its dimensions becomes smaller than three atomic spacings.

Therefore, the increase in catalytic activity as the particles become smaller seems to be a result of changes in the size-dependent electronic structure of the gold. Like other metals, the electrons in gold begin to lose their de-localized character when they approach the nanoscale and the particle eventually undergoes a metal-to-semiconductor-to-insulator transition [7]. This transition occurs because the allowed energy bands in the metal's density of states narrow as the particle becomes smaller and smaller. At a certain point, the thermal energy of the electrons in the metal (approximately = kT) is no longer sufficient to allow the electron to cross the gap between adjacent energy levels and it becomes an insulator. This gap is called the Kubo gap and is defined as:

$$\delta = 4E_f/3N \qquad\qquad (1.3)$$

where $E_f$ is the Fermi energy and N is the number of atoms in the particle. The thermal energy of an electron at room temperature is approximately 25 meV, so that the metal-insulator transition of gold occurs at room temperature when the Kubo gap reaches this value. That happens when the particle consists of approximately 300 atoms. If a hemispherical cap of gold atoms is assumed, this number of atoms will be reached when the particle reaches approximately 2.6 nm in size.

Similarly, gold's color is also dictated by the electronic structure it exhibits. Its characteristic yellowish color is produced by the absorption of light by the 6d-electrons with wavelengths shorter than 496 nm and the reflection of light with wavelengths longer than this value. However, when the particle becomes very small, the critical absorption wavelength increases and gold becomes more reddish in color [8].

4

Finally, the melting point of gold is significantly depressed when it is reduced in size from the bulk to the nano-scale from 1337 K to approximately 800 K due to the increase in the percentage of atoms present on the surface of the particle [9]. So, it is perhaps not as surprising that gold becomes catalytically active when it becomes very small since there are a number of other properties which show similar transitions.

Also well agreed upon is that the method by which the catalyst is synthesized has a strong effect on the catalytic activity displayed. For example, catalysts made by impregnating oxide particles with gold nanoparticles exhibit very low activities whereas those made by simultaneous co-precipitation of gold and the support oxide are highly active [10].

Another well-demonstrated fact is that the choice of oxide support is known to play a key role in the catalytic process. Generally, oxides of the elements in the first row of groups 4-12 in the periodic table have been studied the most, with a strong emphasis on $TiO_2$ and the oxides of iron [11]. Other systems including $Al_2O_3$, $SiO_2$, and $MgO$ have been studied but were found to be less efficient [12]. It should be noted that iron oxide supported catalysts show fundamentally different behavior from the other oxides observed in that a calcination treatment at elevated temperature may not be necessary to bring about high activity.

Such a calcination treatment of the catalysts is usually a major factor determining their performance. Generally, calcination in oxygen tends to improve the stability and activity of the supported gold catalysts, while reduction has very little effect [13]. However, for iron oxide it has been reported that calcination can actually degrade the catalytic performance [14].

## 1.3 Gold Catalysis – What is the Reaction Mechanism?

Unfortunately, here the consensus ends and disagreement begins. One of the most controversial topics is the role that gold in its various oxidation states may play. Some researchers have suggested that only metallic gold ($Au^0$) sites take part in the reaction. Bollinger and Vannice [10] reported a significant increase in activity for CO oxidation when $TiO_x$ overlayers were deposited on an inactive gold powder. This lead them to conclude that the interface of the metallic gold particles and the oxide is the critical active site. Others, like Park and Lee [15], also point towards the role of the interface, but place the emphasis on an oxidized species of gold present there. In their study, they observed the effect of calcination temperature on catalytic activity and found that higher temperatures reduced the activity. Coupling this with XPS and EXAFS studies, they observed the phase transitions from $Au(OH)_3$ to $Au_2O_3$ to metallic gold as the calcination temperature was increased and therefore concluded that the cationic gold species were the active sites. Bond and Thompson [13] later proposed a model that assigned a key role to both species of gold and this will be discussed in greater detail below.

Another unanswered problem concerns the precise role that is played by the oxide support. While most researchers agree that the interface of the gold particle and the oxide support is critical for high activity, the reason that one oxide should be better than another is not well understood. Also, there is speculation that porosity present in the support may play an important part in the reaction. Bond and Thompson have suggested that the reason that calcination processes are often needed is that the co-precipitation synthesis has a tendency to bury the active gold particles within the support. Because of this, they

must be exposed by creating porosity through the loss of water brought about in the calcination treatment [13].

Finally, there exists a debate as to whether or not the presence of highly dispersed gold atoms or tiny clusters of two or three gold atoms plays a significant role in the catalysis. Some researchers have postulated that the highly active species of gold in the reaction are actually much smaller than 3-5 nm. This is particularly true of iron oxide supported catalysts for which Hodge et al [14] found that the highest activities were displayed by the catalysts dried at low temperature. Subsequent electron microscopy analysis failed to detect the presence of gold particles suggesting that they were too small to be resolved with the instrument. Figure 2 shows the differences exhibited by the dried and calcined samples synthesized in their work.



Figure 2 - TEM image of 2.9 at.% Au Iron oxide catalyst prepared via coprecipitation and dried at 120 °C (left) or calcined at 400 °C (right); notice the lack of obvious gold particles in the dried sample [14]

The debate has yet to be settled on this aspect because conventional electron microscopy lacks the resolution necessary to detect individual supported gold atoms or small clusters due to inherent flaws in the magnetic lenses used to focus the electron beam.

must be exposed by creating porosity through the loss of water brought about in the calcination treatment [13].

Finally, there exists a debate as to whether or not the presence of highly dispersed gold atoms or tiny clusters of two or three gold atoms plays a significant role in the catalysis. Some researchers have postulated that the highly active species of gold in the reaction are actually much smaller than 3-5 nm. This is particularly true of iron oxide supported catalysts for which Hodge et al [14] found that the highest activities were displayed by the catalysts dried at low temperature. Subsequent electron microscopy analysis failed to detect the presence of gold particles suggesting that they were too small to be resolved with the instrument. Figure 2 shows the differences exhibited by the dried and calcined samples synthesized in their work.



**Figure 2** - TEM image of 2.9 at.% Au/Iron oxide catalyst prepared via coprecipitation and dried at 120 °C (left) or calcined at 400 °C (right); notice the lack of obvious gold particles in the dried sample [14]

The debate has yet to be settled on this aspect because conventional electron microscopy lacks the resolution necessary to detect individual supported gold atoms or small clusters due to inherent flaws in the magnetic lenses used to focus the electron beam.

## 1.4 Reaction Mechanism – A Proposed Model

Bond and Thompson [13] proposed a model that has found wide use in the field of gold catalysis since it brings together many different researchers' observations and seeks to explain the seeming contradictions that arise. In this model, cationic gold atoms (assumed to be $Au^{III}$) form at the interface between the gold particle and the oxide that binds the two together, while the remainder of the gold consists of metallic $Au^0$ atoms. The ratio of $Au^{III}$ to $Au^0$ can change during heat treatment or reaction, and it is this ratio (and the ratio of $O_2$ to CO used during reaction) that greatly determines the activity of the catalyst.



$$Au^0 + CO \rightarrow Au^0...CO \qquad\qquad (1.4)$$
$$Au^{III} + OH^- \rightarrow Au^{II}...OH \qquad\qquad (1.5)$$
$$Au^0...CO + Au^{II}...OH \rightarrow Au^{II}...COOH + Au^0 \qquad (1.6)$$
$$Au^{II}...COOH + O_2^- \rightarrow Au^{II} + CO_2 + 2OH^- \qquad (1.7)$$
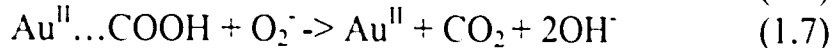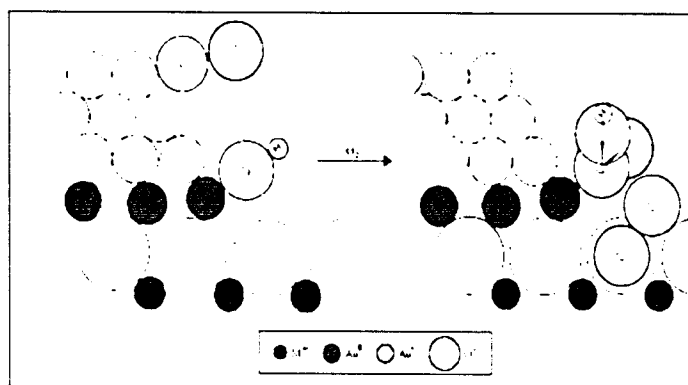
Figure 3 - Schematic of model proposed by Bond and Thompson with summary of reaction steps[13]

According to their model (graphically depicted in Figure 3) the reaction begins by the adsorption of a CO molecule to a $Au^0$ atom. Next, the molecule is attacked by a hydroxyl group that was adsorbed either to a support cation or a $Au^{III}$ periphery atom. The result is a carboxylate group (-COOH) attached to a $Au^{II}$ site. Thirdly, the group is

attacked by a superoxide ion ($O_2^-$) resulting in desorption of a $CO_2$ molecule and a residual hydroxyl group that can then take part in further reaction cycles.

## 1.5 Applications of CO Oxidation

The oxidation of carbon monoxide is of particular interest because there are a wide variety of practical applications for which gold's unique catalytic abilities are ideal. Firstly, the ability of gold to promote CO oxidation at room temperature and below makes it a strong candidate for "cold-start" automotive pollution control. "Cold-start" refers to the period between when an automobile engine is first started and when it reaches the operating temperature of conventional CO oxidation catalysts. Since high temperature oxidation catalysts are readily available and have been for many years, the majority of automobile pollutants are released during the "cold-start" period and, because of the low temperature, are particularly difficult to remove.

Another attractive characteristic of gold catalysts is their high selectivity. This refers to a catalyst's ability to react with one component relative to another. It has been reported that gold shows nearly 100% selectivity for CO oxidation in the presence of $H_2$ [16]. In other words, all of the carbon monoxide is oxidized while any background hydrogen remains undisturbed. This type of selectivity is highly desirable for applications such as hydrogen stream purification for use in polymer membrane fuel cells. Since CO molecules poison the platinum electrode in such devices and render them useless, it is essential that all CO be removed from the hydrogen stream in order for it to function properly. Therefore, the high selectivity for CO oxidation exhibited by gold catalysts could be critical to future fuel cell applications.

9

Finally, gold catalysts have been reported to have exceptional stability compared to other oxidation catalysts. For example, present-day fireman's breathing apparatus are equipped with a $CuMn_2O_4$ (hopcalite) catalyst to oxidize the high concentrations of carbon monoxide present in smoke filled rooms. However, these catalysts have a relatively short lifetime of approximately fifteen minutes after which they are rendered useless by poisoning. In contrast, for comparable atmospheric conditions gold catalysts continue to promote CO oxidation for several hours [17]. Obviously, an increase in the catalyst lifetime would significantly improve the device in which it was being used. Another potential application for this type of low-temperature CO removal is in the space shuttle, where buildup of CO in the shuttle's confined spaces is inevitable due to breath exhalation of the crew.

## 1.6 Effect of Au on ZnO for Methane Oxidation

Methanol is typically synthesized from methane on an industrial scale by a three step process. First, the steam reformation of methane from natural gas is carried out to produce syngas, which contains CO, $H_2$, water, and residual hydrocarbons (Eq. 1.8). Next, the water gas shift is carried out in order to obtain the necessary ratio of $H_2$ to CO (Eq. 1.9). Finally, the CO and $H_2$ are reacted to form $CH_3OH$, methanol (Eq. 1.10). The fact that this process entails three steps increases the cost, so there is great interest in directly forming methanol from the partial oxidation of methane (Eq. 1.11) [18]

$$CH_4 + 2H_2O \rightarrow CO + 3H_2 + H_2O \qquad (1.8)$$

$$CO + H_2O \rightarrow H_2 + CO_2 \qquad (1.9)$$

10

$$CO + 2H_2 \rightarrow CH_3OH \qquad\qquad (1.10)$$

$$2CH_4 + O_2 \rightarrow 2CH_3OH \qquad\qquad (1.11)$$
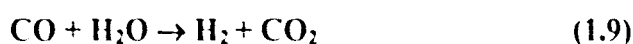
Previous researchers have shown that Cu/ZnO is efficient at catalyzing the

reaction. In particular, Nakamura et al. [19] showed that the size of the supported copper

particles was highly determinative of the catalyst activity. They concluded that the

$Cu^{I}/Cu^{0}$ ratio played a critical role in the catalysis and that the active site was the Cu/ZnO

interface. These findings are remarkably similar to the proposed mechanism for CO

oxidation catalysis by supported gold particles.

Subsequently, Sakurai and Haruta [20] found that dispersed gold nanoparticles on

$TiO_2$ and ZnO were active for catalyzing the direct formation of methanol. They reported

that while the selectivity of $TiO_2$ was better than ZnO, the ZnO catalysts were far better

in terms of methane conversion to methanol. They too reported an increase in activity as

the gold particle size decreased, and hypothesized that this was due to the increased

Au/ZnO interface.


## 1.7 Bi-Metallic Catalysts for $H_2O_2$ Production

In addition to pure nano-sized gold catalysts, it has been found more recently that

the activity of oxide supported palladium particles increases significantly when gold is

added to the system. This behavior was observed in the formation of hydrogen peroxide

by direct combination of hydrogen and oxygen [21]:

$$H_2 + O_2 \rightarrow H_2O_2 \qquad\qquad (1.9)$$

While pure gold was inactive for this reaction and pure palladium was only slightly active, a catalyst formed from precursors of both metals exhibited a significant increase in its activity.

These are particularly striking results because the direct combination reaction is a very simple way of producing hydrogen peroxide. However, it receives scant attention for practical application because it is very difficult to bring about since the same conditions that drive it towards completion also tend to drive the peroxide to dissociate into water just as strongly. Another problem with the reaction is that hydrogen diffuses very quickly out of solution making further reaction impossible. Fortunately, however, carrying out the reaction in a super-critical $CO_2$ solvent sufficiently inhibits diffusion to allow the reaction to proceed [22].

Conventionally, hydrogen peroxide is produced by the reduction and subsequent oxidation of alkyl anthraquinone. There are two inherent drawbacks to this method. First, its by-products are chlorine-based and thus environmentally harmful and must be properly disposed of. Second, because it can only be performed efficiently on a very large scale, only a few highly specialized chemical manufacturers have the capability to cost-effectively synthesize hydrogen peroxide. The subsequent storage and transportation costs drive up the market price. In contrast, there is no capacity problem with the direct combination reaction and its only by-product is water, so that, if the reaction could be successfully promoted with the proper catalyst, the cost of producing hydrogen peroxide would be significantly reduced and the harmful by-products would no longer be produced.

## 1.8 Aims of the Current Study

The goal of this work is to build on the knowledge outlined in the previous sections and to use several catalyst characterization techniques in order to more fully understand the critical variables and the mechanisms that make oxide supported gold such exceptional catalysts.

The first portion of the investigation will involve gold supported on iron oxide particles synthesized using the co-precipitation process for low temperature CO oxidation. Previously, the unique behavior of iron oxide supports relative to others such as $TiO_2$ was outlined. Reviewing briefly, the calcination treatment normally used to activate $TiO_2$ supported catalysts can actually be detrimental to the catalytic activity displayed by iron oxide supported gold. It was postulated that this may be due to the presence of monodisperse gold atoms or to very small clusters of a few gold atoms. Also, there is a possibility that the as formed support particles differ in structure to those that are calcined and this may be a critical component to the increased activity of the uncalcined catalysts.

By using several characterization methods, which will be outlined in the following chapter, the goal of this portion of the study is to more fully understand the nature of the active gold sites in terms of their size and oxidation state and to explain their origin in terms of the processing properties (calcination temperature, time, atmosphere, etc.) used to synthesize them. Also, the structure and role of the oxide support in the process will be investigated to gain a better appreciation of the synergistic effect of combining iron oxide and gold for CO oxidation catalysis.

Finally, similar catalysts will also be examined for their ability to selectively oxidize CO preferentially in an atmosphere containing $H_2$. If the conditions which maximize CO oxidation are not those that produce sufficient selectivity, then it is the goal to determine what the ideal conditions are to maximize both of theses features and to recognize what processing parameters promote them.

The second major portion of the study will examine Au supported on ZnO powder, again synthesized via the co-precipitation process, for use in methane oxidation. In this case, the gold contents will be varied from 0 – 5 at.% and the catalysts will either be calcined at constant temperature or they will simply be dried.

The goal here will be to attempt to understand the effect that gold doping has on ZnO's catalytic activity. Previous studies discussed above have shown that doping with transition metals such as Fe was beneficial to the methane conversion process for reasons that remain somewhat elusive. This study will investigate whether or not gold can have a similar effect on ZnO and attempt to elucidate why this effect is or is not seen.

Finally, the last portion of the study will examine various oxide supports co-impregnated with Au and Pd for producing $H_2O_2$ via direct combination of $H_2$ and $O_2$. The relative contents of Pd and Au will be varied within each set of supports, ranging from pure gold to pure palladium. so that the effect of metal particle composition can be investigated.

Characterization techniques will be employed to examine the structural and compositional nature of the metal particles. For example. do they consist of Au-Pd alloys or are there pure elemental particles of both present. In addition. if the particles are

14

alloyed, the nature of the alloys will be investigated in order to determine whether they are homogeneous or phase-separated.

Finally, while all of the other Au-Pd catalysts examined will be subjected to a calcination and reduction treatment, one uncalcined Au-Pd catalyst will be examined in order to determine the effect on its properties due to thermal history.

# Chapter 2 - Experimental Procedure

Pure gold catalysts with two different oxide supports were examined in this study. These were iron oxide and zinc oxide, and they were chosen specifically because their catalytic activity seems to be controlled by differing mechanisms. For the iron oxide system, the gold content was held constant at either 2.9 or 5 at.% while thermal processing conditions such as calcination temperature, atmosphere, and ramp rates were varied. In contrast, the zinc oxide supported catalysts were all heat-treated under identical conditions but the total gold content was varied systematically from 0 to 5 at.%.

Additionally, three supported Au-Pd bi-metallic catalyst systems were also examined. The catalyst supports compared were iron oxide, aluminum oxide, and titanium oxide. For these samples, the gold and palladium contents were varied systematically within each oxide support group while a consistent thermal treatment was used for all samples.

The following is a detailed description of the preparation, testing, and characterization techniques that were applied to the various catalyst systems.

## 2.1 Catalyst Preparation – Au/Iron Oxide

The iron oxide supported gold catalysts were synthesized by the process of co-precipitation. This was done by mixing dilute aqueous solutions of $HAuCl_4 \cdot 3H_2O$ and $Fe(NO_3)_3 \cdot 9H_2O$ with vigorous stirring (400 rpm) at 50 °C. The pH of the solution was then brought to 8.2 by drop-wise addition of aqueous $Na_2CO_3$ (0.25 mol $l^{-1}$). The Au loading was varied by altering the initial aurochloric acid content of the aqueous solution.

The precipitate which then formed was immediately recovered by filtration and washed

with 1 l of warm deionized water. A small portion of this precipitate was then dried at

room temperature for 24 hours while the remainder was dried at 120 °C in air for sixteen

hours.

Table 2.1 - Summary of Au/Iron oxide catalyst systems investigated for low temperature CO oxidation
(all Au loadings determined to be 2.9 at.%)

| Sample ID | Calcination Temp. (°C) | Calcination Time (hrs.) | Atmospheric Conditions |
|-----------|------------------------|-------------------------|------------------------|
| 12 | - | - | Dried in Air |
| 12.1 | 70 | 8 | Static Air |
| 12.2 | 120 | 8 | Static Air |
| 12.3 | 200 | 8 | Static Air |
| 12.4 | 300 | 8 | Static Air |
| 14.1 | 120 | 8 | Static Air |
| 14.2 | 120 | 8 | Circulated Air |
| 15.1 | 120 | 8 | Circulated Air |
| 24 | 120 | 8 | Circulated Air |
| 24.1 | 120 | 8 | Static Air |

Table 2.2 - Summary of Au/Iron oxide catalysts investigated for CO oxidation in the presence of $H_2$
(all Au loadings are 5 at.%)

| Sample ID | Calcination Temperature (°C) | Calcination Time (hrs.) |
|-----------|------------------------------|-------------------------|
| 25.1 | 120 | 8 |
| 25.2 | 400 | 3 |
| 25.3 | 400 then 550 | 3 |
| 25.4 | 550 | 3 |
| 25.5 | 600 | 3 |

After drying, the product was ground to a fine powder prior to pelleting at a

pressure of 10 torr. The pellets were crushed and sieved to the required mesh size for

catalytic testing in a 150-250 μm microreactor. Portions of the product that were dried at

120 °C were subsequently calcined at various temperatures ranging from 200 °C – 600 °C for three hours in static air. Refer to Tables 2.1 and 2.2 for a complete listing of all the iron oxide samples and their corresponding processing histories.

## 2.2 Catalyst Preparation – Au/ZnO

The zinc oxide supported catalysts were prepared by a similar co-precipitation process except that the $Fe(NO_3)_3 \cdot 9H_2O$ component was replaced by $Zn(NO_3)_2$. The gold content was systematically varied from 0 – 5 at% by altering the proportion of aurochloric acid to give the desired loading. Again, all samples were then dried at 120 °C in air for approximately sixteen hours. Half of the zinc oxide samples were then calcined at 500 °C for five hours in static air. Table 2.3 shows a summary of all ZnO samples used in this study.

Table 2.3 - Summary of Au/Zinc oxide catalysts examined for methane oxidation

| Sample ID | Gold Loading (at.%) | Calcination Temp. (°C) | Calcination Time (hrs.) |
|---|---|---|---|
| Z0 | - | Uncalcined | - |
| Z1 | 1 | Uncalcined | - |
| Z2 | 2 | Uncalcined | - |
| Z5 | 5 | Uncalcined | - |
| ZC0 | - | 500 | 5 |
| ZC1 | 1 | 500 | 5 |
| ZC2 | 2 | 500 | 5 |
| ZC5 | 5 | 500 | 5 |

## 2.3 Catalyst Preparation – $H_2O_2$ Catalysts

All of the samples used for hydrogen peroxide production were synthesized by impregnation via an incipient wetness process. This was done by constantly stirring pre-prepared oxide support particles (haematite, alumina, or titania) in aqueous solutions of $Pd(NO_3)_2 \cdot 6H_2O$ and $HAuCl_4 \cdot 3H_2O$ for four hours. The gold/palladium content of each catalyst was varied by controlling the relative concentrations of the two aqueous solutions. The product was then recovered via filtration and dried in air at 120 °C for sixteen hours. The majority of the samples were subsequently calcined for three hours in air at 400 °C. However, a portion of the Au-Pd/$TiO_2$ samples was retained after drying without further heat treatment. Table 2.4 is a summary of all the catalysts examined for $H_2O_2$ production.

Table 2.4 - Summary of Au-Pd catalysts investigated for $H_2O_2$ production

| Sample ID | Support Material | Palladium Loading (at.%) | Gold Loading (at.%) |
|---|---|---|---|
| APA1 | Alumina | - | 5 |
| APA2 | Alumina | 2.5 | 2.5 |
| APA3 | Alumina | 5 | - |
| APF1 | Haematite | - | 5 |
| APF2 | Haematite | 2.5 | 2.5 |
| APF3 | Haematite | 5 | - |
| APT1 | Titania | - | 5 |
| APT2 | Titania | 1 | 4 |
| APT3 | Titania | 2.5 | 2.5 |
| APT4 | Titania | 5 | - |

## 2.4 Catalyst Testing

The catalyst testing for all of the samples examined in this work was performed at Cardiff University by Dr. Graham Hutchings and his research group. All CO oxidation reactions were performed in a fixed bed laboratory microreactor under standard conditions. Typically, this means CO (5% in He, 5 ml min$^{-1}$) and $O_2$ (50 ml min$^{-1}$) were fed to the reactor at controlled feed rates using mass flow controllers, and passed over 50 mg of catalyst at 20 °C. The reaction products were analyzed using on-line gas chromatography.

In addition to the atmospheric conditions described above, the iron oxide supported samples that contained the higher gold loading (5 at.%) were tested for CO selectivity in the presence of $H_2$. The testing conditions were similar except that $H_2$ was introduced with a 2:1 molar ratio of $H_2$:$O_2$. Flow conditions for this reaction were: CO (0.1 ml/min), $H_2$ (0.2 ml/min), $O_2$ (4 ml/min), and $N_2$ (20.7 ml/min) with a total gas hourly space velocity (GHSV) of 3000 h$^{-1}$.

The zinc oxide supported catalysts were observed for direct methanol synthesis by partial oxidation of methane in an inert helium atmosphere. The reaction was carried out in a similar fashion except that flow conditions were: $CH_4$ (23 ml/min), $O_2$ (2 ml/min), and He (5 ml/min) over 0.25 cm$^3$ of catalyst.

Catalytic testing of all samples for hydrogen peroxide synthesis was performed using a Parr Instruments stainless steel autoclave with a nominal value of 50 ml and a maximum working pressure of 14 MPa. The autoclave was equipped with an overhead stirrer (0-2000 rpm) and the capability for measurement of temperature and pressure.

Typically, 0.05 g of catalyst was added to the autoclave and purged three times with $CO_2$ (3 MPa) and then filled with 5 wt.% $H_2/CO_2$ and 25 wt.% $O_2/CO_2$. $CO_2$ was then added to a total pressure of 9.2 MPa using a Milton Roy dosing pump. Stirring (1200 rpm) was started on reaching the desired temperature (2 °C) and experiments were run for 30 min. Gas analysis for $H_2$ and $O_2$ was performed on line by gas chromatography using a thermal conductivity detector and a CP-Carboplot P7 column (25 m, 0.53 mm id). Conversion of $H_2$ was calculated by gas analysis before and after reaction. $H_2O_2$ yield was determined by titration of aliquots of the final filtered solution with acidified $Cd(SO_4)_2$ ($7 \times 10^{-3}$ mol $l^{-1}$). $Ce(SO_4)_2$ solutions were standardized against $(NH_4)_2Fe(SO_4)_2 \cdot 6H_2O$ using ferroin as an indicator.

## 2.5 Catalyst Characterization

In order to more fully understand the origins of gold's unique catalytic abilities, the goal of this study was to utilize a wide variety of characterization methods to investigate several catalyst systems. These methods were X-ray photoelectron spectroscopy (XPS), extended X-ray absorption fine structure (EXAFS) and X-ray absorption near-edge structure (XANES), and transmission electron microscopy (TEM). The following is a description of each of these methods and their uses in catalyst characterization in addition to specific details about the instruments and the experiments carried out on them.

### 2.5.1 Catalyst Characterization - Transmission Electron Microscopy

The nanoscopic size of gold catalyst particles dictates that a microscopy technique capable of resolving structures that are less than a few nanometers in size is necessary to properly characterize them. Transmission Electron Microscopy (TEM) is ideally suited to this task since it is capable of much higher resolutions than Scanning Electron Microscopy (SEM), and because the irregular surfaces of real catalysts make them unsuitable for analysis by Scanning Probe Microscopy (SPM) techniques such as STM and AFM.

In TEM, a high-energy beam of electrons is produced either by thermionic emission from a source such as $LaB_6$ or tungsten or field emission from a source such as tungsten. This beam is directed at the sample via magnetic lenses, which can predictably deflect the beam. The sample must be thin enough so that the beam can pass through without being completely absorbed by the specimen. Once the beam passes through the specimen, it is directed onto an imaging device, usually a photo-luminescent screen or a digital imaging camera. In the case of catalyst powders, they are by their very nature already this thin and it only remains to disperse them on a suitable grid in order to limit flocculation.

The ability of the TEM to resolve extremely small particles is limited by the size of the electron beam. Theoretically, an instrument operating at 200 kV should produce a probe size of 0.003 nm according to the de Broglie relationship. However, due to the nature of magnetic lenses, there are several inherent aberrations that cause the

beam to spread and thus reduce the resolution. The most serious of these aberrations is

known as spherical aberration, and is a result of the axial distance dependence on the

field strength of the lens. Because electrons that are closer to the optic axis are further

away from the lens, they will encounter a smaller magnetic deflecting force than those

electrons near the perimeter of the lens. These outer electrons will be deflected to a

larger degree than the axial electrons, and the beam will therefore broaden. The result is

that a point will be imaged as a disk of finite size depending on the degree to which this

effect is limited in the instrument. A ray diagram that exaggerates the effect of spherical

aberration is depicted in Figure 4. The rays near the perimeter are deflected more than

those more near the center of the lens, and the result is a broadened beam at $F_1$.
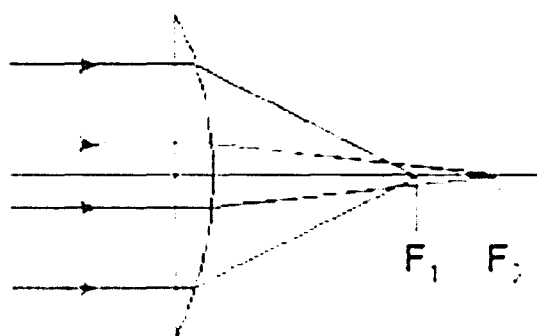


Figure 4 - Exaggerated ray diagram showing origin of spherical aberration

The minimum probe size due to spherical aberration can be calculated by:

$$r_{min} = 0.91(C_s\lambda^3)^{1/4} \qquad (2.1)$$

where $C_s$ is the spherical aberration coefficient of the lens and $r_{min}$ is the practical

resolution of the instrument. The best TEM instruments have a value of $r_{min}$ that is

approximately 0.15 nm [23].

In addition to imaging, TEM and its' variants: scanning transmission electron microscopy (STEM), analytical electron microscopy (AEM), etc. can also be utilized for many other useful applications such as diffraction and compositional analysis.

Samples of all catalysts were prepared for electron microscopy by grinding with a mortar and pestle and dispersing each in high purity ethanol. Then a drop of the suspension was allowed to evaporate on a holey-carbon film supported by a 300 mesh copper grid.

Transmission electron microscopy (TEM) was performed on a JEOL 2000 FX operating at 200 kV for low magnification (< 500 kX) imaging and electron diffraction analysis. Selected area diffraction (SAD) patterns using a highly underfocused, nearly parallel electron beam were taken from areas containing multiple particles by using a relatively large SAD aperture. The resulting polycrystalline ring pattern could be used for structural identity of the oxide support. This was accomplished by measuring the ratio of each ring radius to that of the smallest ring radius. The resulting ring pattern ratio sequences were then matched to the theoretical crystal structure exhibited by the oxide. For higher gold loadings, the contribution to the diffraction pattern of the gold was considered as well. For interpretation of these results, model crystal structures and XRD patterns were produced using CaRIne v. 3.1 [24], a commercial crystallography program.

Imaging with the JEOL 2000 FX, while useful, is limited by the low intensity of the $LaB_6$ electron source and the relatively large aberrations present in the objective lens. The point-to-point resolution, under optimum conditions, is approximately 0.3 nm or $3 \times 10^{-10}$ m.

For higher resolution imaging, a JEOL 2010F FEG TEM operating at 200 kV and equipped with a Gatan Image Filter (GIF) was used. The improved lens system in the JEOL 2010F significantly reduces the effects of spherical aberration and improves the resolution of the instrument. This improvement in resolution and the high-coherency of the beam produced by the FEG source can be utilized to produce lattice plane images. This technique is commonly referred to as high-resolution (or HRTEM) imaging. Lattice planes are resolved by allowing multiple electron beams to contribute to the image rather than isolating a single incident or diffracted beam, as in bright or dark field imaging. The multiple beams interact with each other producing an interference pattern that, under the proper conditions, is directly representative of the atomic plane periodicity within the material. This technique can be used to identify particular crystal structures, orientations, and defects, but the interpretability of the results are highly dependent on specimen thickness and the degree of beam underfocus. In addition, conventional imaging benefits greatly from the improved lens system. In the case of the JEOL 2010F, the point to point resolution is approximately 0.2 nm or $2 \times 10^{-10}$ m.

Additionally, annular dark field (ADF) imaging was done on the JEOL 2010F in scanning transmission electron microscopy (STEM) mode, wherein the beam is rastered across the surface of the specimen rather than remaining stationary. This mode was especially suited for this task since the gold particles appeared as bright spots against a dark background and this aided in image interpretation.

High-angle annular dark field (HAADF) imaging was performed on a VG Systems HB603 STEM operating at 300 kV with a FEG source. This technique can be used to form images with very strong atomic number (Z) contrast. Conventional electron

diffraction by atomic planes occurs at very small angles; typically less than 20 mrads.

However, elastic Rutherford scattering of fast electrons by single atoms can cause

angular deflections of a much larger magnitude [23]. To create an image with these types

of scattered beams, the beam is rastered across the surface of the specimen and an image

signal is captured at each point on the sample using an annular detector, which collects all

electrons deflected from the optic axis by more than 50 mrads. Since the ease of

scattering is determined by the highly Z-sensitive cross-section of the atoms present, the

image contrast will likewise be highly sensitive to atomic number differences. For an

example relevant to this discussion, gold (Z = 79) atoms will appear much brighter than

iron or zinc (Z = 26 and 30 respectively) in the resulting image due to the larger

scattering cross-section of gold. A schematic diagram illustrating the HAADF technique

is shown in Figure 5.

Rastered Beam

Specimen

HAADF Detector
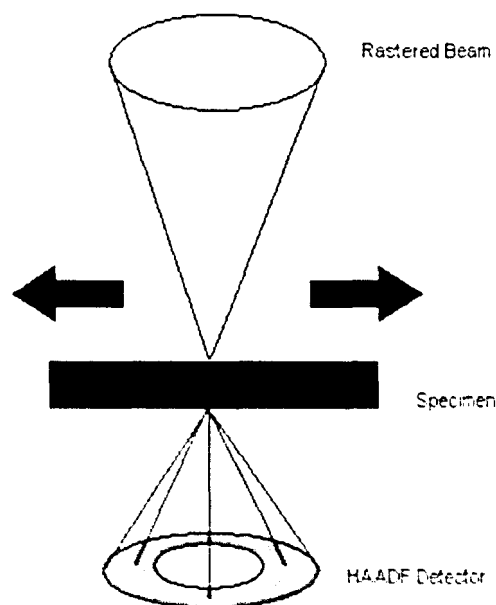
Figure 5 - Schematic diagram of the HAADF imaging technique

All image analysis, whether on the VG 603 or the JEOL systems, was performed using Gatan Digital Micrograph v. 3.6.5 [25], a widely available imaging software package that permits feature size measurements, Fourier analysis, and image thresholding among other useful techniques.

Additionally, the STEM was equipped with an Oxford Instruments INCA TEM 300 system for energy dispersive X-ray spectroscopy (XEDS) analysis [26]. With this system, a digital X-ray signal was collected at each point, or pixel, of the beam raster. This makes possible the formation of an X-ray map of the image where the specific elemental composition of each point is known. The sensitivity of these maps is determined by the dwell time of the beam. For a longer dwell time, the number of X-ray counts produced from one pixel of the scan raster increases, and thus the ability of the instrument to detect more minute traces is improved. However, increasing the dwell time also increases the collection time and enhances the beam damage produced from the 300 kV incident beam. In addition, the presence of specimen drift will be exaggerated for longer collection times resulting in distorted maps. Therefore, it was sometimes necessary for practical purposes to use a lower dwell time of 50 – 100 microseconds, but wherever possible a dwell time of 200 microseconds was chosen. When a shorter dwell time was used, the acquired maps were subsequently processed using a computational technique known as multi-variant statistical analysis (MSA), which reduced the effects of signal noise [27]. Finally, point and line analysis of the XEDS data is also made possible with the INCA software.

## 2.5.2 Catalyst Characterization – X-ray Photoelectron Spectroscopy (XPS)

XPS has been widely used for surface characterization of materials for the last couple of decades. Since the relative depth of analysis is no greater than a few nanometers, XPS can provide essential information about the chemistry of a specific surface used in catalytic reactions, such as the oxidation state of surface atoms and type of bonding between them [28]. An XPS spectrometer detects the electrons that are ejected from a specimen surface when illuminated with X-ray beam photons with energies in the keV range. Part of the energy of the incident beam (equal to $h\upsilon$, the photon energy) is then transferred to the electrons as their kinetic energy $E_k$, according to the equation:

$$h\upsilon = E_k + E_b + \Phi \qquad (2.3)$$

In this equation $E_b$ is the binding energy required to take an electron from a particular energy level to the Fermi level and $\Phi$ is the work function of the material under examination.

The binding energy of the emitted electrons can be determined from this equation, and qualitative as well as quantitative surface composition analysis is possible from the resulting data. However, it should again be emphasized that this technique is highly surface sensitive even though the X-rays penetrate the material rather easily. This is due to the low energy of the emitted electrons, which does not permit their escape from depths of more than a few nanometers. Therefore, XPS results are not necessarily indicative of bulk characteristics.

While XPS has a tremendous surface sensitivity, allowing analysis of only the first few nanometers of the material's surface, its minimum spatial resolution is well above 10 microns. Therefore, it is an insufficient technique for analysis of individual nanosized gold and gold alloy particles such as those contained in catalysts. However, XPS is a powerful tool for determining the overall properties of an ensemble of particles.

The generation of photoelectrons requires the whole system to be under ultra high-vacuum conditions, making the XPS equipment rather expensive. However, XPS has been established as one of the major surface analytical techniques, especially in the field of catalysis.

For this investigation, XPS spectra were recorded on a VG ESCA-Lab 220I spectrometer, using a standard Al $K_\alpha$ X-ray source (300 W) and an analyzer pass energy of 20 eV. Samples were mounted using double-sided adhesive tape and binding energies are referenced to the C(1s) binding energy of adventitious carbon contamination which is taken to be 284.7 eV. The effective cross-sections used for the calculation were obtained by Scofield based on solution of the Dirac equation [29].

For the $Au/Fe_2O_3$ samples, the binding energy shift of the Au(4d) peak relative to the C(1s) electrons were measured. As a check, the Au(4d)-Fe(2p) and Au(4d)-O(1s) shifts were also measured.

The bi-metallic catalysts were also examined using XPS in order to determine the surface gold and palladium composition of each catalyst. This was done by measuring the intensity ratio of the Pd(3d) to the Au(4d$_{5/2}$) peaks. This ratio is then correlated to a sample of known composition in order to calculate the composition of the unknown.

### 2.5.3 Catalyst Characterization – Extended X-ray Absorption Fine Structure (EXAFS) and X-ray Absorption Near-Edge Structure (XANES)

Extended X-ray Absorption Fine Structure (EXAFS) and X-ray Absorption Near Edge Structure (XANES) are X-ray spectroscopy techniques that can be used to, among other things, determine oxidation states of constituent elements, the nature of adsorbed gas molecules, and local structural information such as coordination numbers. A monochromatic X-ray beam is directed at the sample. The photon energy of the incident X-ray are gradually increased such that it traverses one of the absorption edges of the elements contained within the sample. Below the absorption edge the corresponding electrons cannot be excited by the incident photons, and thus absorption is low. However, when the photon energy is just sufficient to excite the electrons to the vacuum level then a large increase in absorption occurs known as the absorption edge. The resulting photoelectrons have a low kinetic energy and can be backscattered by the atoms surrounding the emitting atom. The probability of backscattering is dependent on the energy of the photoelectrons, and the backscattering of the photoelectron affects whether the X-ray photon is absorbed in the first place. Hence, the probability of X-ray absorption will depend on the X-ray photon energy, as the photoelectron energy will depend on the photon energy. The net result is a series of oscillations on the high photon energy side of the absorption edge. These oscillations can be used to determine the atomic number, interatomic distance and coordination number of the atoms surrounding the element whose absorption edge is being examined. It must be specified that backscattering from only one atom is considered in EXAFS data.

However, XANES data is collected with very low energy photons and, because of this, scattering from more than one atom can take place. This type of scattering occurs with at least three scattering atoms (the absorbing atom and the two scattering atoms), and thus gives structural information about triplet and higher coordinations. Since these techniques require an X-ray source that can produce a wide-range of energies, synchrotron radiation is most often used in practice [30].

X-ray absorption experiments were performed on beamline X-18B of the National Synchrotron Light Source (NSLS) at Brookhaven National Laboratoryby the research group of Dr. Bruce Gates (University of California-Davis). Data were recorded at the Au $L_{III}$ edge before and during CO oxidation catalysis. For the in-situ analysis, the samples were tested with flowing mixtures of CO and $O_2$ (CO partial pressure, $P_{CO}$ = 11-220 Torr and $O_2$ partial pressure, $P_{O_2}$ = 11-220 Torr; the remainder He) at atmospheric pressure and temperature of 373 K.

# Chapter 3 – Results and Discussion

The following chapter will present the results of the experimental investigation carried out for the various catalyst systems and discuss their implications. The pure Au/Iron oxide for low-temperature and selective CO oxidation will be discussed first. Subsequently, the results of the Au/Zinc oxide catalysts for methane conversion will be examined, and, finally, the results of the Au-Pd bi-metallic catalysts for hydrogen peroxide production will be interpreted.

## 3.1 Au/Iron Oxide Catalysts for Low Temperature CO Oxidation

This first section concerns the pure Au/Iron Oxide catalysts for low-temperature CO oxidation. The primary focus of this part of the investigation was to build on previous knowledge of gold catalysis by further clarifying the nature of the reaction and the components that make it possible. These included the species of gold involved ($Au^0$, $Au^I$, $Au^{III}$, etc.), the role played by the oxide support, and the processing variables that enhance catalytic activity.

### 3.1.1 Catalytic Testing Results

It is apparent from the data collected in Table 3.1 that the method used to prepare these catalysts has an obvious effect on their catalytic performance. For example, the dried samples (i.e. those heat treated below 200 °C) generally were very effective catalysts, even reaching CO conversions of 100 % in some cases. Surprisingly, one of the best catalysts at 66% CO conversion was sample 12, which was simply allowed to dry at room temperature. In contrast, the calcined samples (those heat treated at 200 °C and above) were not nearly as efficient at converting CO to $CO_2$. Samples 12.3 and 12.4 were only able to convert 7 and 26% of the carbon monoxide, respectively, making them two of the poorest catalysts.

In previous studies of $Au/TiO_2$ catalysts it was reported that a calcination treatment at elevated temperature was an essential step in producing a good catalyst [1]. Since such a heat treatment increases the degree of support-particle interaction and it is believed that this interaction in part brings about the activity of the catalyst, samples that were not calcined tended to have very low activities.

**Table 3.1** - Catalytic Testing Results for Au/Iron Oxide Samples

For Low Temperature CO Oxidation

| Sample ID | CO Conversion % | Calcination Temp. ($^{o}$C) |
|:---:|:---:|:---:|
| 12 | 66 | - |
| 12.1 | 32 | 70 |
| 12.2 | 65 | 120 |
| 12.3 | 7 | 200 |
| 12.4 | 26 | 300 |
| 14.1 | 0 | 120 |
| 14.2 | 100 | 120 |
| 15.1 | 94 | 120 |
| 24 | 100 | 120 |
| 24.1 | 0 | 120 |

However, for these Au/Iron oxide catalysts the opposite effect is clearly observed. More specifically, if only the catalytic activities of the dried samples are considered, there is also a great deal of fluctuation in their ability to catalyze the reaction depending on the furnace used for the heat treatments. For example, samples 14.2, 15.1, and 24 were all dried at 120 °C in a gas chromatography (GC) oven, and they all showed consistently high CO conversion percentages (near 100% in all three cases). However, samples 14.1 and 24.1 were also dried at 120 °C, but the drying was done in a tube furnace. These two catalysts were unable to convert any of the CO to $CO_2$ making them the two poorest catalysts in the entire group. This drastic difference in catalytic activity from one furnace to another can only be the result of two variables, as all other conditions were consistent from one furnace to the next. These variables are the temperature ramp rate and the atmospheric flow conditions of the furnace. In the GC oven, the oven was allowed to reach 120 °C before the sample was inserted, but in the tube furnace the

sample was inserted when the unit was at room temperature. This makes the effective ramp rate of the GC oven much higher than the 5 °C/min. of the tube furnace. In addition, the GC oven operates with an atmosphere of constantly flowing air, while in the tube furnace the atmosphere is static air. Therefore, it appears that one of these two variables (or perhaps both) is critical to the performance of the resulting catalyst.

## 3.1.2 XRD Results

XRD analysis results from an early study of pure gold on iron oxide supports are shown in Figure 6 [14]. In this study, the gold content was varied from sample to sample so that sample C contained the most gold, followed by sample B, and sample A contained the least. These samples were then each divided and one half was dried at 120°C and the other was calcined at 300 °C. The spectra reveal little if any difference between the samples due to their gold contents, but they data does show the distinct differences between the dried and calcined samples. In the dried sample, there are no clear peaks shown in the spectrum. Instead there are broad humps that cannot be indexed to any particular crystal structure. This suggests a considerable amount of structural disorder present in the support material, which is to be expected since the drying temperature was not high enough to produce significant atomic rearrangement for crystallization and growth.
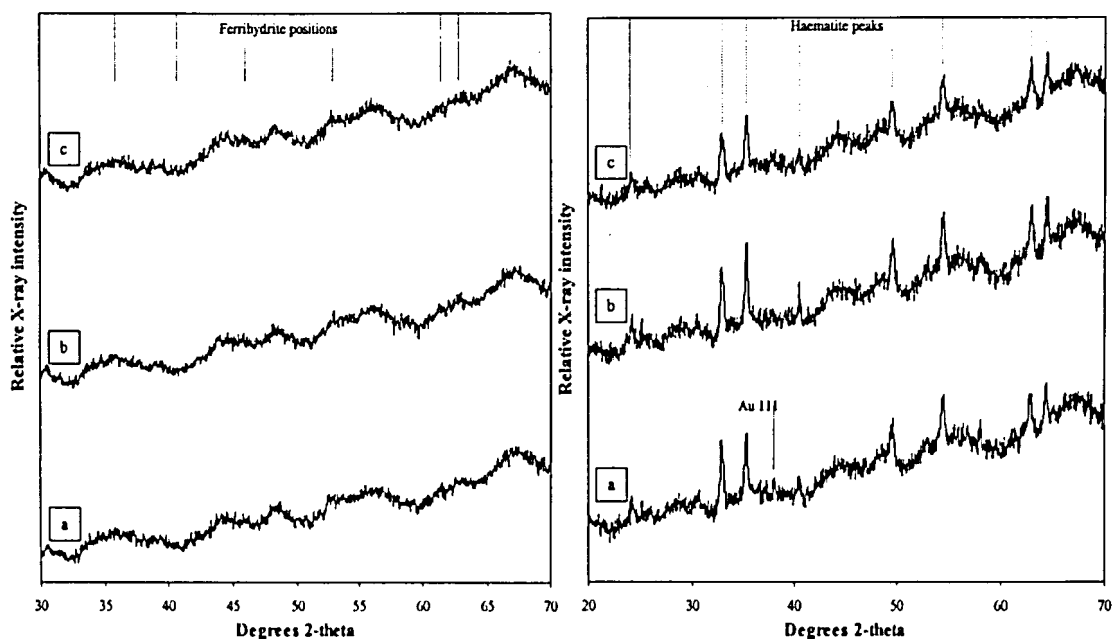
**Figure 6** - XRD patterns of Au/Iron oxide catalysts; left dried at 120 °C, right calcined at 300 °C [14]

The XRD spectra obtained from the calcined samples are quite different. The spectrum for the calcined sample in Figure 6 contains well-defined peaks that can definitively be assigned to $\alpha$-$Fe_2O_3$ or haematite, which has the corundum crystal structure. A schematic of the $Fe_2O_3$ crystal structure is shown in Figure 7. There is also the possibility of a very tiny gold peak, which is labeled in the spectrum. These results show that the calcined catalysts contain well- crystallized haematite support particles, which are generated by the elevated heat treatment temperature.

**Figure 7** – Schematic diagram of the haematite ($Fe_2O_3$) crystal structure, iron = purple, oxygen - red

Therefore, it seems clear that the catalysts with high activity exhibit a more disordered oxide-support structure that cannot be clearly assigned to any of the iron oxide or oxy-hydroxide morphologies by XRD. In contrast, the poorer catalysts contain well-crystallized haematite support particles.

### 3.1.3 XPS Results

In Figure 8, a plot of the Au(4d)-C(1s) binding energy difference measured via XPS vs. CO conversion percentage is shown. The plot shows a general trend that suggests that the more efficient catalysts have a larger binding energy difference. This is confirmed by the data collected in Appendix A for the Au(4d)-Fe(2p) and Au(4d)-O(1s) binding energy differences.

**Figure 7** – Schematic diagram of the haematite ($Fe_2O_3$) crystal structure, iron = purple. oxygen - red

Therefore, it seems clear that the catalysts with high activity exhibit a more disordered oxide-support structure that cannot be clearly assigned to any of the iron oxide or oxy-hydroxide morphologies by XRD. In contrast, the poorer catalysts contain well-crystallized haematite support particles.

### 3.1.3 XPS Results

In Figure 8, a plot of the Au(4d)-C(1s) binding energy difference measured via XPS vs. CO conversion percentage is shown. The plot shows a general trend that suggests that the more efficient catalysts have a larger binding energy difference. This is confirmed by the data collected in Appendix A for the Au(4d)-Fe(2p) and Au(4d)-O(1s) binding energy differences.

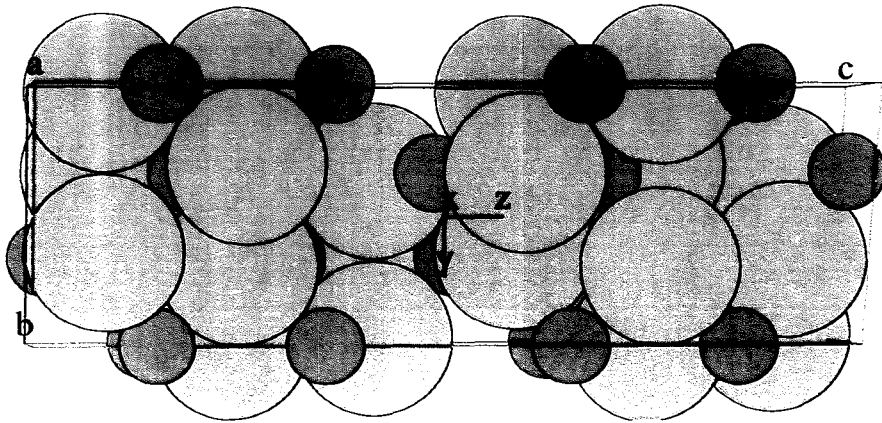**Figure 8** - Catalytic activity vs. Au(4d)-C(1s) binding energy difference for Au/Iron oxide catalysts

The binding energy difference in this case can be used as a measure of the magnitude of the particle-support interaction since a stronger interaction will produce a larger binding energy shift. Since the highest CO conversions generally were obtained with catalysts that also exhibited a large binding energy difference, the data suggests that a strong interaction is beneficial to the catalytic process. Similarly, Bond and Thompson [13] suggested that a strong particle support interaction is beneficial to the performance of the catalyst in the $Au/TiO_2$ system. However, in contrast to titania supported catalysts, it appears that the particle-support interaction for Au/Iron oxide is actually weakened by the calcination process at higher temperatures, as evidenced by the larger B.E. differences exhibited by the dried samples. For example, the BE difference for sample 14.2 (dried, high activity) and 12.3 (calcined, low activity) differ by 1.3 eV, which is a very significant deviation when XPS results are concerned.
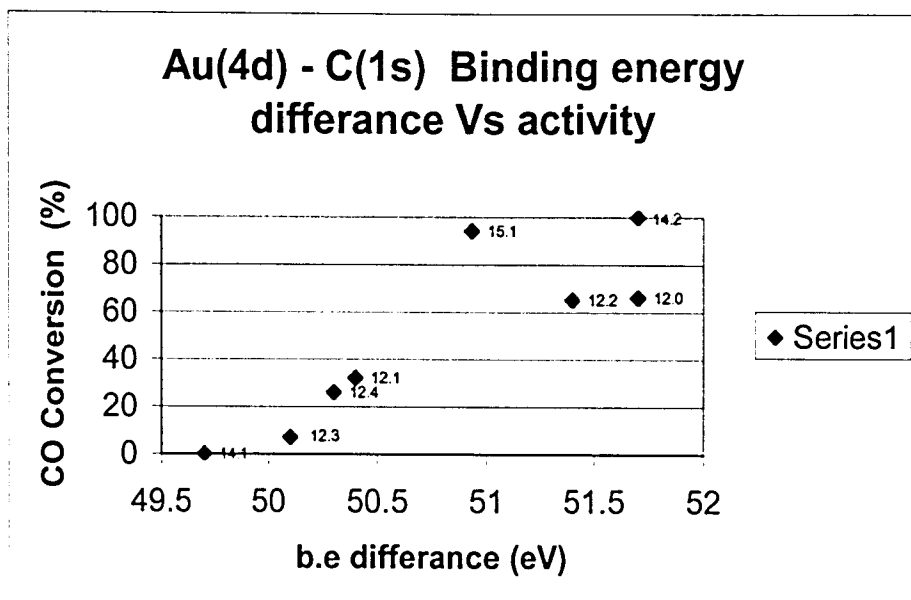
**Figure 8** - Catalytic activity vs. Au(4d)-C(1s) binding energy difference for Au/Iron oxide catalysts

The binding energy difference in this case can be used as a measure of the magnitude of the particle-support interaction since a stronger interaction will produce a larger binding energy shift. Since the highest CO conversions generally were obtained with catalysts that also exhibited a large binding energy difference, the data suggests that a strong interaction is beneficial to the catalytic process. Similarly, Bond and Thompson [13] suggested that a strong particle support interaction is beneficial to the performance of the catalyst in the $Au/TiO_2$ system. However, in contrast to titania supported catalysts, it appears that the particle-support interaction for Au/Iron oxide is actually weakened by the calcination process at higher temperatures, as evidenced by the larger B.E. differences exhibited by the dried samples. For example, the BE difference for sample 14.2 (dried, high activity) and 12.3 (calcined, low activity) differ by 1.3 eV, which is a very significant deviation when XPS results are concerned.
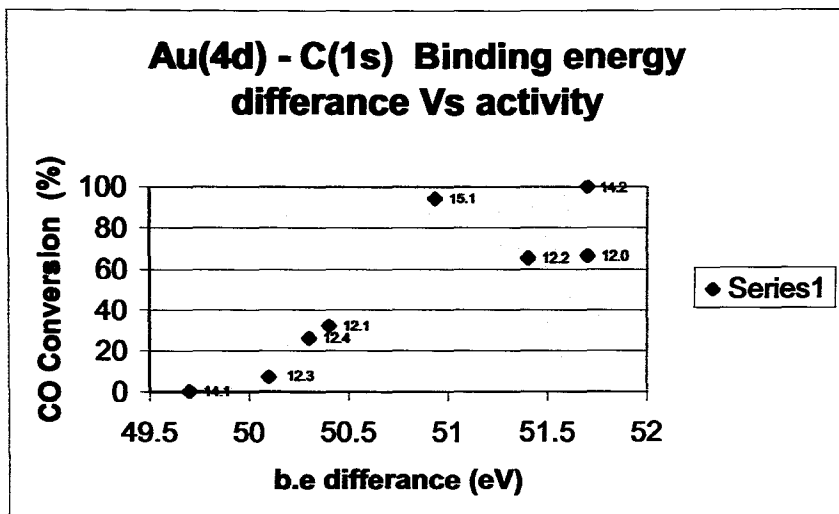
37

This also suggests that a suitable preliminary measure of the activity of a gold catalyst for CO oxidation would be XPS measurements of the Au(4d) binding energy measured relative to some reference binding energy transition, which is usually most conveniently the C(1s) electron in the contamination layer.

### 3.1.4 EXAFS and XANES Results

The in-situ EXAFS results compiled in Tables 3.2a and 3.2b clearly show a new Au-C shell formed during the reaction that was not present in the inert helium atmosphere. This suggests the presence of CO molecules adsorbed onto metallic gold sites in the catalyst, which is completely in keeping with the Bond and Thompson model. The fit parameters used for this data are shown in Appendix A.

Table 3.2a – EXAFS results characterizing the $Fe_2O_3$-supported gold sample dried at 120 °C; in inert He and during CO oxidation catalysis at 298 K and a pressure of 760 Torr

| | treatment gas | | | | | | | |
|---|---|---|---|---|---|---|---|---|
| | He | | | | $CO + O_2 + He$ | | | |
| backscatterer | $N$ | $R$ (Å) | $10^3 \times \Delta\sigma^2$ (Å$^2$) | $\Delta E_0$ (eV) | $N$ | $R$ (Å) | $10^3 \times \Delta\sigma^2$ (Å$^2$) | $\Delta E_0$ (eV) |
| Au–Au 1$^{st}$ shell | 8.2 | 2.80 | 7.31 | 1.27 | 7.8 | 2.80 | 8.92 | 1.30 |
| Au–Au 2$^{nd}$ shell | 4.0 | 3.90 | 8.45 | 4.61 | 4.5 | 4.01 | 12.99 | 8.62 |
| Au–O$_s$ | 1.4 | 2.04 | 2.36 | 4.67 | 0.7 | 2.10 | 0.51 | 3.85 |
| Au–O$_l$ | 1.1 | 2.60 | 2.63 | -1.23 | 0.8 | 2.62 | -0.45 | -2.48 |
| Au–C | – | – | – | – | 0.9 | 1.81 | 6.20 | 0.44 |

**Table 3.2b** – EXAFS results characterizing the $Fe_2O_3$-supported gold sample calcined at 300 °C; in inert He and during CO oxidation catalysis at 298 K and a pressure of 760 Torr

| backscatterer | treatment gas |
| | \multicolumn{4}{c}{He} | \multicolumn{4}{c}{$CO + O_2 + He$} |
| | $N$ | $R$ (Å) | $10^3 \times \Delta\sigma^2$ (Å$^2$) | $\Delta E_0$ (eV) | $N$ | $R$ (Å) | $10^3 \times \Delta\sigma^2$ (Å$^2$) | $\Delta E_0$ (eV) |
|---|---|---|---|---|---|---|---|---|
| Au–Au 1$^{st}$ shell | 10.7 | 2.85 | 10.12 | 2.98 | 10.4 | 2.84 | 9.93 | 2.08 |
| Au–Au 2$^{nd}$ shell | 5.9 | 4.01 | 12.52 | 7.87 | 5.8 | 4.06 | 11.73 | 9.94 |
| Au–O$_s$ | 0.7 | 2.08 | 2.18 | 7.99 | 0.9 | 2.08 | 1.38 | 6.92 |
| Au–O$_l$ | 0.5 | 2.62 | 3.84 | -4.92 | 0.6 | 2.55 | 0.90 | 0.48 |
| Au–C | – | – | – | – | 0.9 | 1.78 | 8.88 | 0.84 |

The XANES data plotted in Figure 9 show another striking difference between the dried and calcined samples. The high-activity, dried sample exhibits a sharp peak near 11920 eV, while the calcined sample shows only a weak bump in this vicinity. Also, the higher energy region of the spectrum for the dried sample shows only broad bumps while for the calcined sample there are much more clearly delineated peaks in the spectrum near 11945 and 11970 eV. This suggests a clear difference in the electronic nature of the gold particles in the two catalyst samples. Since the peak near 11920 eV is typical of cationic gold (most likely Au$^+$) and the higher energy peaks are typical of metallic Au$^0$ [31], this suggests that the dried samples contain primarily cationic gold and the calcined samples contain primarily metallic gold species.

This change in the oxidation state of the gold atoms is most likely a result of the interaction between the metal particles and the oxide support. These observations correlate well with the XPS results discussed above.
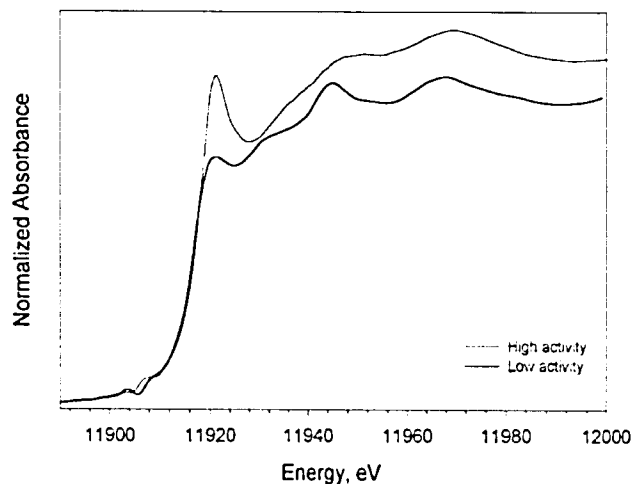
**Figure 9** - XANES data for the Au/Iron oxide for low temperature CO oxidation: dried at 120 °C (high activity; red line) and the calcined at 300 °C (low activity; black line).

However, these gold cations are extremely unstable and reduce very rapidly to $Au^0$ as the temperature is elevated, thus the metallic nature of the particles in the calcined sample. Additionally, the cationic nature of the particles undergoes a metallic transition as the particles grow larger than approximately 3 nm, which is the very scale of the particles in question.

Finally, Figure 10 shows the XANES data taken in-situ during the room temperature CO oxidation. This data clearly shows that the electronic character of the gold particles remains constant throughout, and is not altered by the catalytic process for a period of at least one hour. However, the same differences noted in the previous XANES spectra continue to exist between the dried and calcined sample throughout the reaction process.
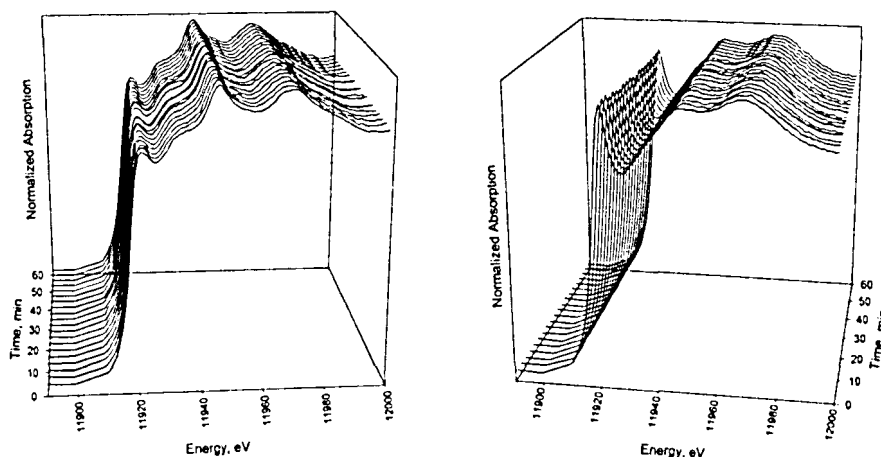
**Figure 10** - Transient in-situ XANES data characterizing the calcined gold/iron oxide catalysts (left) and the dried catalyst (right) during CO oxidation catalysis

### 3.1.5 Electron Microscopy Results

Selected area diffraction (SAD) pattern analysis suggested that the support structure of all of the examined samples was found to be $\alpha$-$Fe_2O_3$, or haematite, regardless of heat treatment. Also, there are two low-intensity peaks present in the calcined sample that are absent from the dried samples that can be assigned to the gold (111) and (200) reflections. The experimental and theoretical data used for this determination are collected in Appendix B. Figure 11 shows the difference between the diffraction pattern produced by a dried and a calcined sample. The pattern produced by the calcined sample is "spotty" such that the diffraction rings are not continuous, while the uncalcined sample creates a pattern with unbroken, but broad circles. This could be due to the size difference of the oxide particles present in each sample. The support particles would be expected to be larger in the calcined samples than those in the

41

uncalcined samples due to sintering and grain growth. The larger size reduces the number of support particles in the sampling area that contribute to the diffraction pattern, so that, statistically, there are not enough reflections present to complete the rings.

Also noticeable is the increased width of the rings obtained from the uncalcined samples compared to the calcined sample. This occurs because the support particles in this case are so small that they are much closer in size to the electron beam than the particles in the calcined samples. Therefore, the detectability limit of the instrument is being approached, and the rings begin to broaden. Further reducing the particles in size would eventually cause the rings to broaden into disks and, finally, to lose all relevant information entirely.



**Figure 11** - SAD ring pattern of Au Iron oxide calcined at 300 °C (left) and dried at 120 °C (right) [C.L. = 200 cm]

This electron diffraction data differs from the findings of the XRD analysis, which did not indicate the presence of haematite in the dried samples but rather a highly

42

uncalcined samples due to sintering and grain growth. The larger size reduces the number of support particles in the sampling area that contribute to the diffraction pattern, so that, statistically, there are not enough reflections present to complete the rings.

Also noticeable is the increased width of the rings obtained from the uncalcined samples compared to the calcined sample. This occurs because the support particles in this case are so small that they are much closer in size to the electron beam than the particles in the calcined samples. Therefore, the detectability limit of the instrument is being approached, and the rings begin to broaden. Further reducing the particles in size would eventually cause the rings to broaden into disks and, finally, to lose all relevant information entirely.
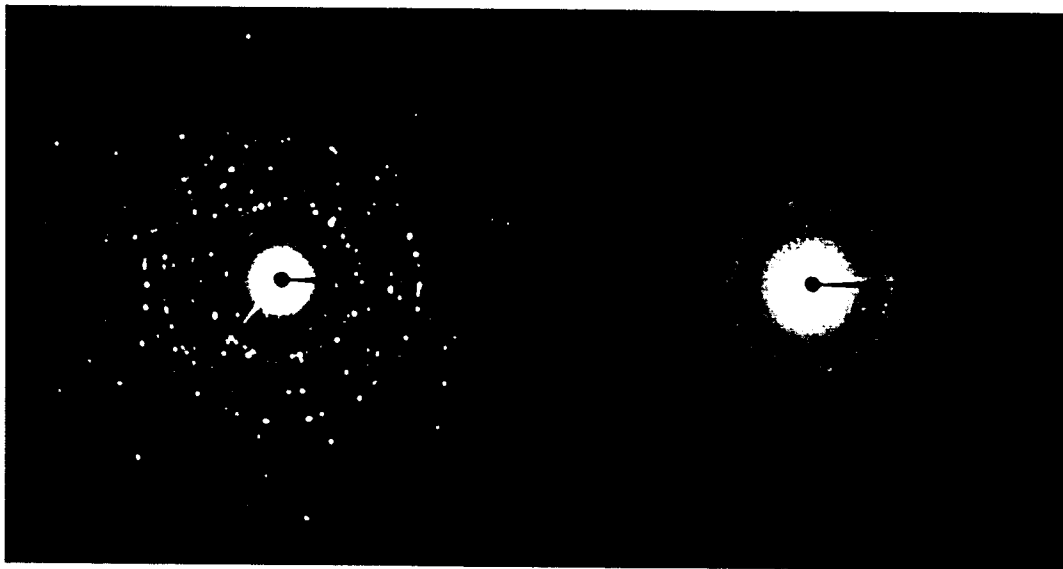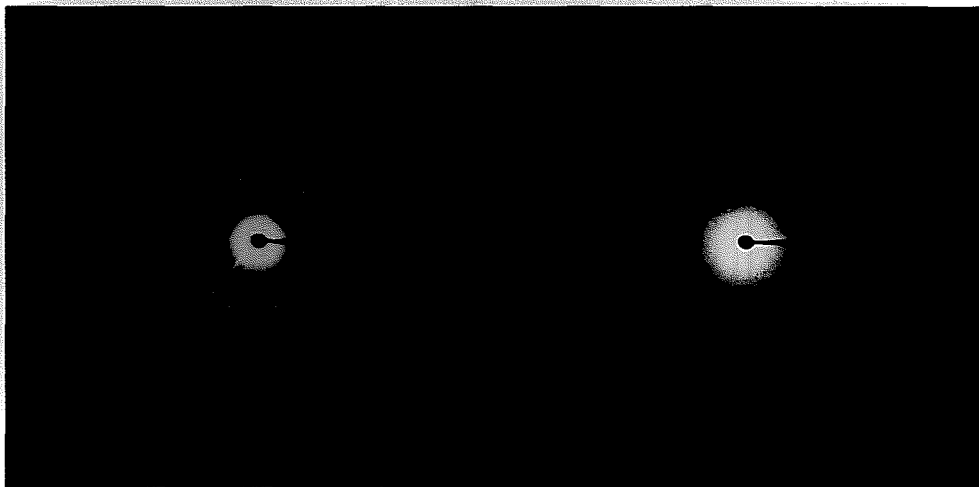


**Figure 11** - SAD ring pattern of Au/Iron oxide calcined at 300 °C (left) and dried at 120 °C (right) [C.L. = 200 cm]

This electron diffraction data differs from the findings of the XRD analysis, which did not indicate the presence of haematite in the dried samples but rather a highly

disordered structure. The explanation for this contradiction is similar to that of the ring broadening in the electron diffraction patterns discussed above. X-ray diffraction, while an ideal technique for bulk analysis, loses its effectiveness as the particles being observed become smaller and smaller. As this happens, the spectrum peaks begin to broaden until they are completely lost in the signal background. This certainly explains the lack of gold peaks present in the spectra, but it can also explain the absence of iron oxide or oxy-hydroxide peaks in the dried sample's data since the support particles in this case are less than 10 nm in size. In contrast, electron diffraction is much more suitable to structural determination of particles of this size since the theoretical wavelength of the electron beam (0.003 nm for 200 keV electrons) is two orders of magnitude less than that of the X-ray beam (.154 nm for a $CuK_\alpha$ source). However, in practice, the electron beam is much larger due to the presence of lens aberrations. See section 2.5.1 for details on the specific resolutions of the instruments used.

The measured particle size data for these samples is presented in Table 3.3. Typically, an average value was taken from fifty particle measurements. The sequence of images in Figure 12 shows that the heat treatment temperature has a significant effect on the catalyst's structure. For instance, the images of the sample calcined at 300 °C show well-crystallized oxide particles that can be as large as 40 nm in size. Also obvious in these images are rather large gold particles that stand out clearly as very dark regions against the oxide particle background due to increased mass-thickness scattering by the heavy gold atoms.

Table 3.3 - Summary of gold and oxide particle size measurements for CO oxidation catalysts

| Sample ID | Au Particle Size (nm) | Oxide Particle Size (nm) | Calcination Temp. (°C) |
|-----------|------------------------|---------------------------|-------------------------|
| 12 | * | 6.0 – 16.1 | - |
| 12.1 | * | 7.5 – 19.2 | 70 |
| 12.2 | 2.1 | 7.4 - 18.7 | 120 |
| 12.3 | 5.9 | 7.5 – 24.2 | 200 |
| 12.4 | 6.8 | 8.3 - 37.5 | 300 |
| 14.1 | 7.0 | 5.1 – 16.3 | 120 |
| 14.2 | 5.4 | 7.9 – 20.2 | 120 |
| 15.1 | * | 4.5 – 27.3 | 120 |
| 24 | 2.6 | 7.5 | 120 |
| 24.1 | 3.5 | 36 | 120 |

\* - Gold particles could not be resolved in these samples

In contrast, the images of the dried samples show a highly disordered oxide structure containing very small particles as well as regions with a layered, needle-like morphology. The gold is not nearly as visible in these uncalcined samples, and a higher magnification is necessary to resolve the particles, which are approximately 2-3 nm in size. HAADF STEM imaging with the VG HB 603 was sufficient for this task in most samples, and Figure 13 shows these very small gold particles in a HAADF image as well as an accompanying $AuM_2$ XEDS map for a typical dried and calcined sample pair. However, for samples 12, 12.1, and 15.1 no gold particles were resolved at all even in HAADF imaging. This is a possible indication that they are so small (< 1 nm) that they are beyond the resolution of the instrument.

Needle-like Morphology

Figure 12 - TEM bright-field images showing how the morphology changes with calcination temperature. Dried at room temperature (Top Left 300 kX), calcined at 200 °C (Top Right 300 kX), and calcined at 300 °C (Bottom, 800 kX)

Some difference in gold particle size is apparent, to varying degrees, between all the dried and calcined samples. Therefore, a simple conclusion about the iron oxide system can be made that the best catalysts tend to contain the smallest gold particles, while the larger particles produced at an elevated calcination temperature are less efficient at catalyzing the CO oxidation reaction.

45

**Figure 12** - TEM bright-field images showing how the morphology changes with calcination temperature. Dried at room temperature (Top Left 300 kX), calcined at 200 $^{0}$C (Top Right 300 kX), and calcined at 300 $^{\circ}$C (Bottom, 800 kX)

Some difference in gold particle size is apparent, to varying degrees, between all the dried and calcined samples. Therefore, a simple conclusion about the iron oxide system can be made that the best catalysts tend to contain the smallest gold particles, while the larger particles produced at an elevated calcination temperature are less efficient at catalyzing the CO oxidation reaction.

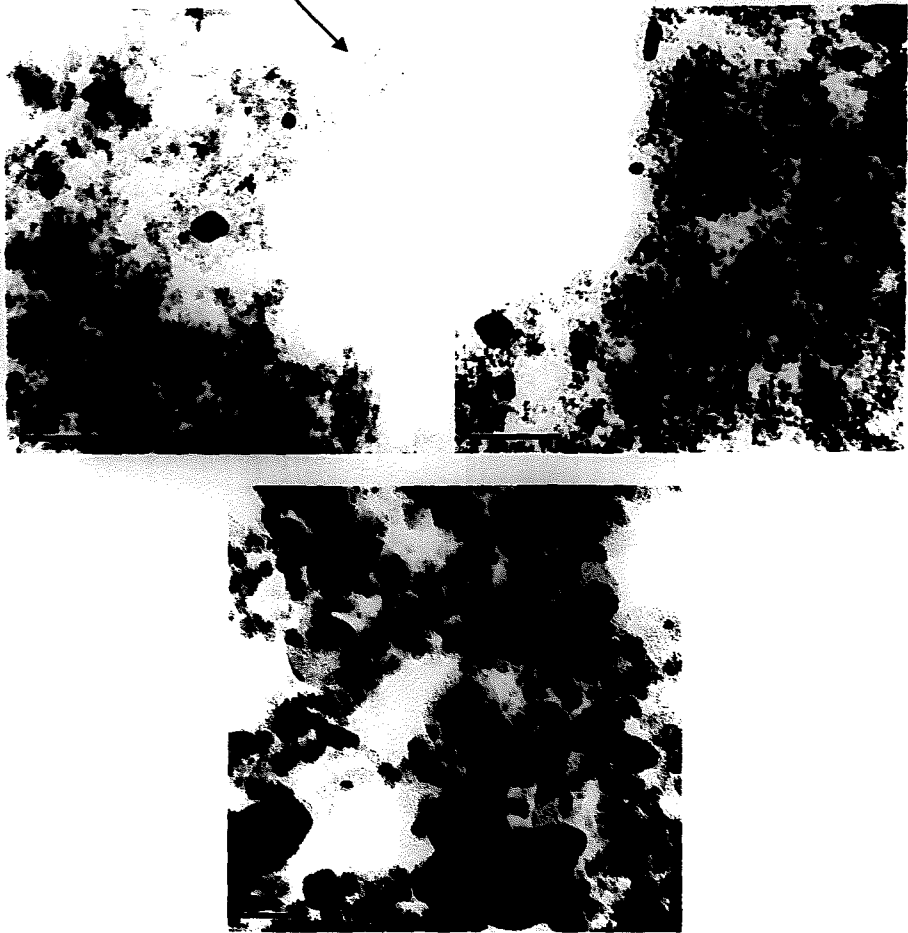**Figure 13** - HAADF images and corresponding XEDS maps of the Au $M_2$ signal for samples 14.2 (top) and 14.1 (bottom) [200 kX, 100 μs Dwell Time]

However, the structure of the oxide support also plays a key role as evidenced by the clear link between a high catalytic activity and a heat treatment temperature of 120 °C or less. The catalysts dried at these temperatures consisted of very small support particles surrounded by disordered regions as well as areas possessing a layered morphology. The catalysts that were calcined at 200 °C and above were all poor catalysts, and contained large well-crystallized haematite particles. Therefore, the smaller support particles and the layered morphology are beneficial to the reaction process.

This increasing size of the oxide support particles with calcination temperature is to be expected. The melting temperature of iron oxide is 1565 °C so significant bulk
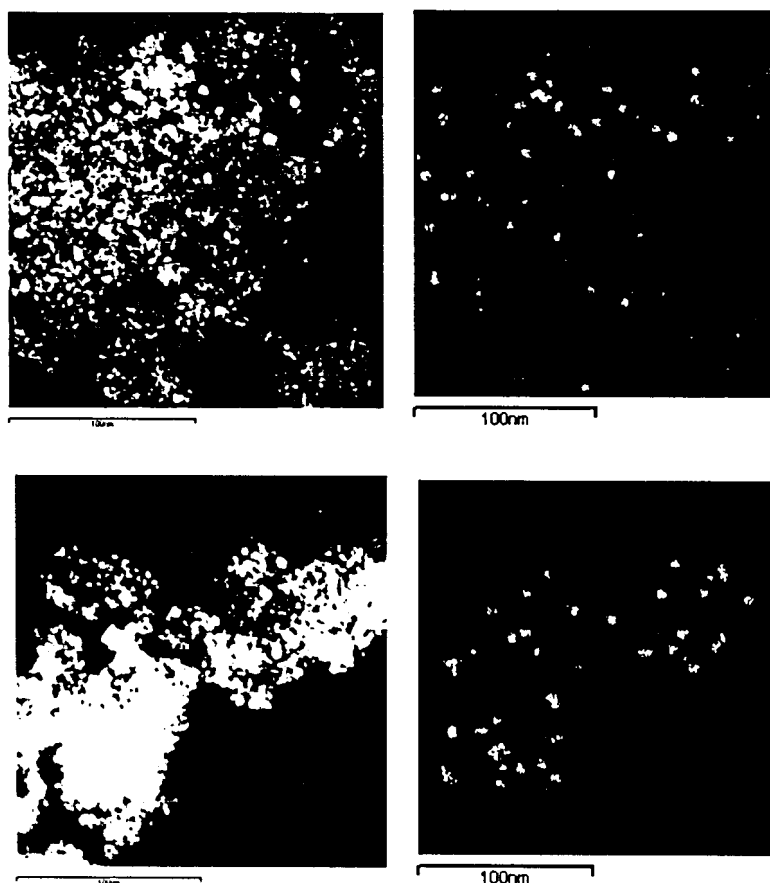
**Figure 13** - HAADF images and corresponding XEDS maps of the Au $M_2$ signal for samples 14.2 (top) and 14.1 (bottom) [200 kX, 100 µs Dwell Time]

However, the structure of the oxide support also plays a key role as evidenced by the clear link between a high catalytic activity and a heat treatment temperature of 120 °C or less. The catalysts dried at these temperatures consisted of very small support particles surrounded by disordered regions as well as areas possessing a layered morphology. The catalysts that were calcined at 200 °C and above were all poor catalysts, and contained large well-crystallized haematite particles. Therefore, the smaller support particles and the layered morphology are beneficial to the reaction process.

This increasing size of the oxide support particles with calcination temperature is to be expected. The melting temperature of iron oxide is 1565 °C so significant bulk
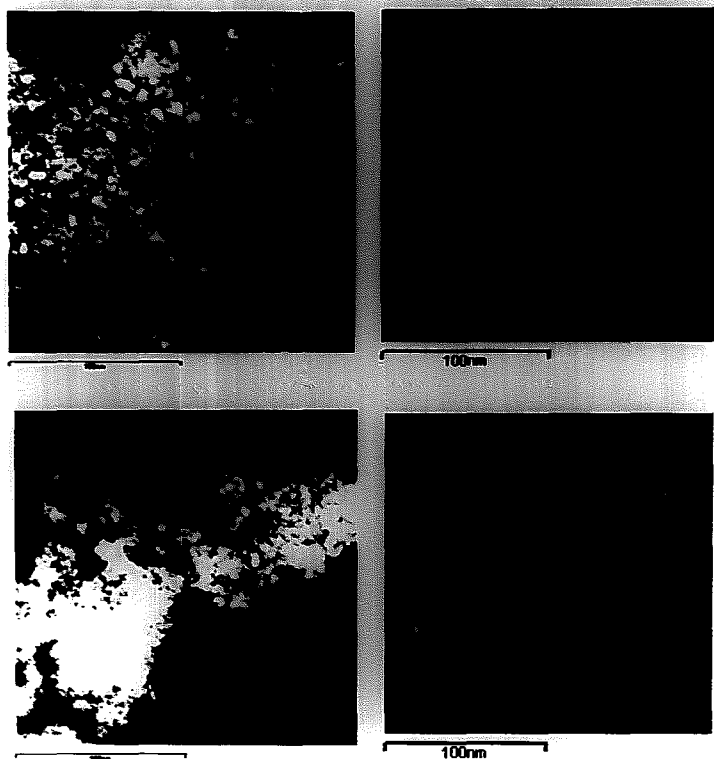
diffusion should be expected only above 500 °C [32]. However, since the smallest

support particles are approximately 7 nm in size prior to heat treatment, their high surface

area provides a large driving force for sintering and particle growth can occur at much

lower temperatures.

The layered areas of the uncalcined samples were suspected to be goethite

(FeO(OH)), a common low temperature oxy-hydroxide of iron at low temperatures that

forms needle-like structures similar to those seen in earlier micrographs. However,

electron diffraction analysis was insufficient for definitively identifying them as such

because goethite exhibits only three strong reflections all of which occupy angular

positions very near intense haematite peaks, as shown below in Table 3.4.

Table 3.4 – Strongly reflecting goethite and haematite peaks showing proximity

| Haematite XRD Peaks | | Goethite XRD Peaks | |
|---|---|---|---|
| hkl | 2θ Value | hkl | 2θ Value |
| 1 0 -2 | 36.3 | 1 0 1 | 31.8 |
| 1 0 4 | 50.3 | 3 0 1 | 50.4 |
| 2 -1 0 | 54.3 | 1 1 1 | 55.9 |

* Calculated for theoretical X-rays (Lambda = 2.3 Angstroms)

Also, convergent beam diffraction analysis was impossible because the particles

were not stable enough to withstand a converged 200 keV electron beam. Therefore,

electron diffraction techniques were not sufficient for determining the crystal structure of

these layered regions. However, goethite typically shows a layered or needle-like shape

as shown in Figure 14, which may explain the appearance of these regions in the electron

micrographs. A computer-generated image of the structure of goethite is also shown in Figure 15.
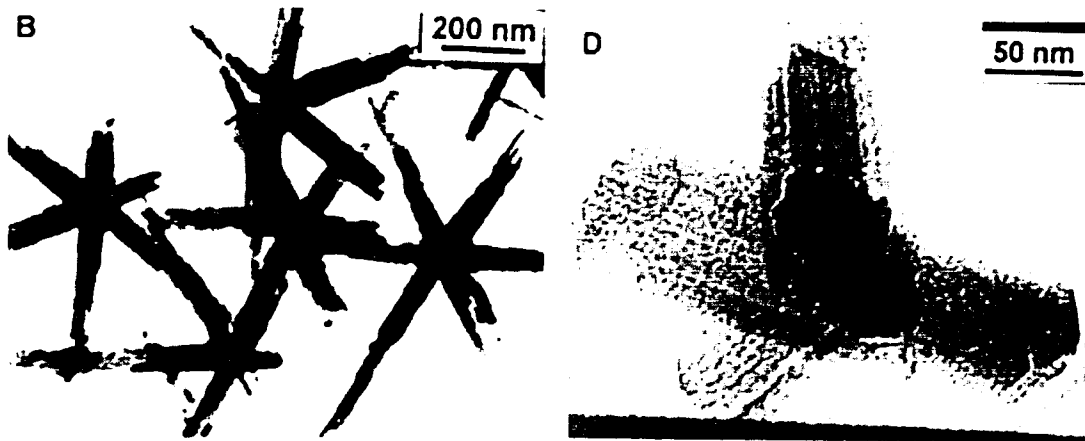


**Figure 14** - Electron micrographs of typical morphology of goethite prepared from ferrihydrite [100kX] [133]

Goethite begins decomposing at approximately 200 °C [34], therefore the observation that the samples calcined at 200 °C and above do not contain the layered morphology correlates with the physical properties of goethite.
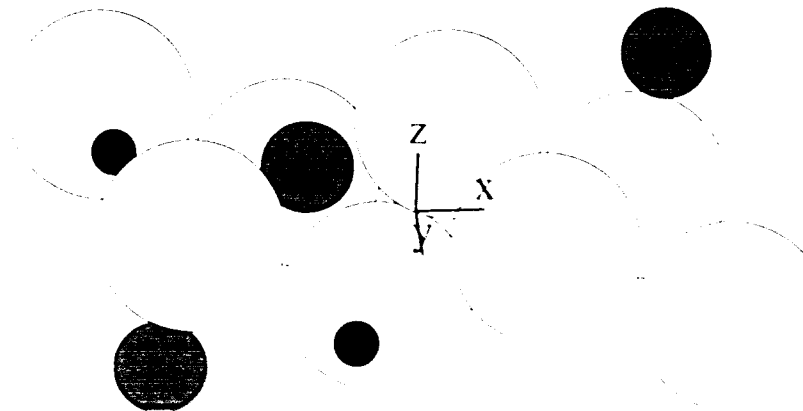


**Figure 15** – Schematic diagram of the structure of goethite, FeO(OH). Iron = red, oxygen = yellow, hydrogen = blue

Finally, electron micrographs of samples 24 and 24.1 are shown in Figure 16(a) and (b), respectively. Since these two samples were both dried at 120 °C, the structures were expected to be similar. However, the TEM images reveal that the two catalysts are actually quite dissimilar. Most notably, sample 24.1, which was dried in the tube furnace under static air conditions, has undergone a significantly greater amount of sintering and growth of the oxide and gold particles than sample 24, which was dried under constant flowing air in a GC oven.



Figure 16 – Transmission Electron Micrographs of samples 24 (left) and 24.1 (right), 300 kX

Since only the temperature ramp rate and atmospheric flow conditions were altered between the two heat treatments, one or both of these variables appears to be critical in controlling the size and structure of the resulting catalyst and, consequentially, its ability to promote the oxidation reaction. Also, the average gold particle diameters observed were larger for the poorer catalyst but they were still well below the supposed

Finally, electron micrographs of samples 24 and 24.1 are shown in Figure 16(a) and (b), respectively. Since these two samples were both dried at 120 °C, the structures were expected to be similar. However, the TEM images reveal that the two catalysts are actually quite dissimilar. Most notably, sample 24.1, which was dried in the tube furnace under static air conditions, has undergone a significantly greater amount of sintering and growth of the oxide and gold particles than sample 24, which was dried under constant flowing air in a GC oven.
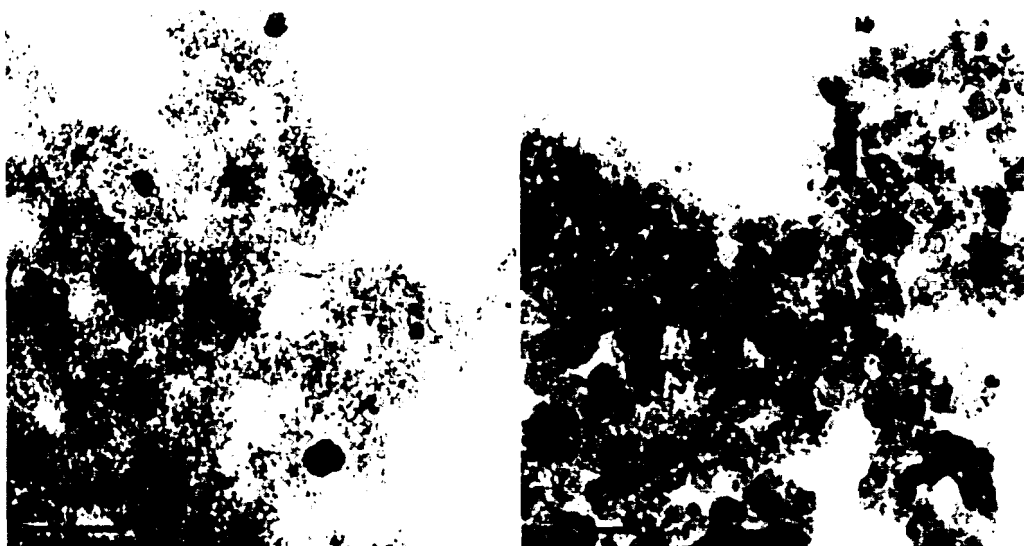


**Figure 16** – Transmission Electron Micrographs of samples 24 (left) and 24.1 (right), 300 kX

Since only the temperature ramp rate and atmospheric flow conditions were altered between the two heat treatments, one or both of these variables appears to be critical in controlling the size and structure of the resulting catalyst and, consequentially, its ability to promote the oxidation reaction. Also, the average gold particle diameters observed were larger for the poorer catalyst but they were still well below the supposed

threshold of 5 nm. However, the oxide particles were not only larger, but possessed none of the disordered, goethite-type morphology present in the high activity catalyst. Again, this points towards the critical and unique role played by the iron oxide support in this system.


## 3.1.6 Summary of Au/Iron Oxide for Low Temperature CO Oxidation

In summary, Au/Iron oxide catalysts can be synthesized that are remarkably active for CO oxidation at room temperature and even below. However, the processing steps taken during synthesis are critical to the performance of the resulting catalyst. In order to produce a highly active catalyst, the heat treatment temperature must be low in order to avoid particle growth of the gold particles. EXAFS and XANES suggest that such a heat treatment reduces the percent of ionic gold species present in the catalyst by increasing the gold particle size and allowing them to oxidize to metallic $Au^0$ atoms. This supports the contested notion that the presence of ionic gold atoms in the catalyst greatly enhances its activity.

XPS analysis also revealed a loose correlation between high catalytic activity and a strong Au(4d) electron binding energy. This suggests that a strong particle support interaction is desirable for improving catalytic performance and that the calcined samples tended to possess a lower binding energy than the as dried samples.

A low temperature heat treatment also avoids crystallization and sintering of the oxide support particles. If the oxide particles are heated to a level where sintering is possible the goethite-type layered structure will decompose to equiaxed haematite particles, and the catalytic performance is hindered.

Finally, the atmospheric flow conditions and/or the furnace ramp rate used during the heat treatment has a strong effect. Static air conditions and a slow ramp rate combine to promote the decomposition of goethite to haematite and cause the growth of the oxide particles, while a constantly flowing atmosphere and a high ramp rate minimize these two phenomena.

## 3.2 Au/Iron Oxide for Selective Oxidation of CO in the Presence of $H_2$

The next section will present the results of an investigation carried out on catalysts much like those discussed above. However, in this case, the goal was to elucidate the conditions and variables that would improve the selectivity of the catalysts to CO oxidation relative to $H_2$ conversion. Primarily, an attempt was made to discover the best processing variables that produced a catalyst that would efficiently oxidize CO while not disturbing any of the $H_2$ present in the atmosphere. After this, the successful and unsuccessful catalysts were examined to determine the nature of their performance and its relation to their processing histories.

### 3.2.1 Catalytic Testing Results

In Table 3.5, the catalytic testing results for the second group of Au/Iron oxide samples show that the calcination treatment and the reaction temperature used during catalytic testing greatly affect the activity and selectivity of the catalyst.

**Table 3.5** - Catalytic testing results of Au/Iron Oxide for selective CO oxidation in the presence of $H_2$

| Sample ID | Calcination Temperature (°C) | CO Conversion % | | | $H_2$ Conversion % | | |
|---|---|---|---|---|---|---|---|
| | | 27°C | 50 °C | 73 °C | 27°C | 50 °C | 73 °C |
| 25.1 | 120 | 85 | 85 | 85 | 5 | 35 | 80 |
| 25.2 | 400 | 68 | 84 | 91 | 0 | 0 | 0 |
| 25.3 | 400 then 550 | 37 | 71 | 80 | 0 | 0 | 5 |
| 25.4 | 550 | 12 | 19 | 37 | 0 | 0 | 0 |
| 25.5 | 600 | 0 | 0 | 0 | 0 | 0 | 0 |

The first obvious trend is that as the calcination temperature is raised, the ability of the catalyst to oxidize CO is progressively reduced. This is in keeping with the results reported in section 3.1 on low temperature CO oxidation.

Second, increasing the reaction temperature increases the activity of the catalyst for all cases except the two extreme cases of samples 25.1 and 25.5. This is to be expected since the added thermal energy to the system contributes to overcoming the energy barrier to reaction. In the case of sample 25.1, a relatively high CO conversion value (85%) is maintained at all temperatures, which suggests that the catalyst so efficiently lowers the energy barrier for oxidation that the increased reaction temperature has a negligible effect. This is in contrast to sample 25.5, which is such a poor catalyst that even the increased reaction temperature is not sufficient to allow the reaction to proceed.

Finally, the results show that, with the exception of sample 25.1, these catalysts are extremely selective to CO oxidation in the presence of $H_2$, even at elevated temperature. Sample 25.1, which happens to exhibit the highest level of CO conversion, shows the greatest tendency to convert $H_2$ to $H_2O$, even at low temperature. This suggests that the mechanism of CO conversion is also weakly operative for $H_2$

conversion, and it is only by reducing the ability of the catalyst to oxidize CO via a suitable calcination treatment that the selectivity is increased.

### 3.2.2 Electron Microscopy Results

Electron diffraction analysis shows that all of the catalyst samples' supports exhibit the corundum-like haematite structure. This is in keeping with the observations found for the previous group of Au/Iron oxide catalysts.

Table 3.6 - Particle size data for Au/Iron oxide catalysts for CO oxidation in $H_2$

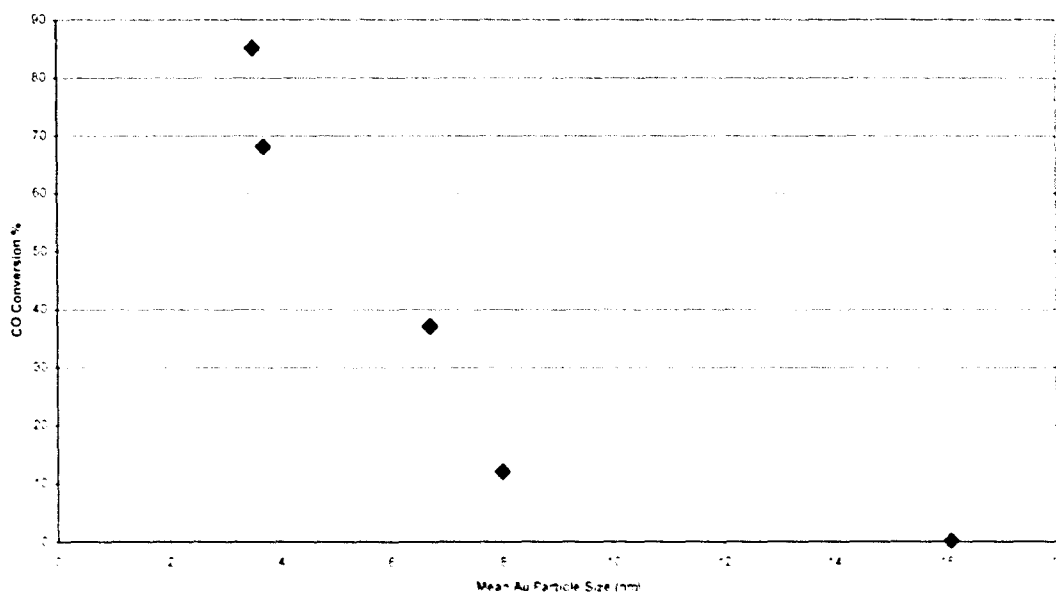| Sample ID | Calcination Temperature ($^o$C) | Au Particle Size (nm) | Oxide Particle Size (nm) |
|-----------|---------------------------------|-----------------------|--------------------------|
| 25.1 | 120 | 1.1 | 9.1 |
| 25.2 | 400 | 3.7 | 14.3 |
| 25.3 | 400 then 550 | 6.7 | 38.5 |
| 25.4 | 550 | 8.0 | 36.2 |
| 25.5 | 600 | 16.1 | 81.2 |



Figure 17 - CO conversion % vs. mean Au particle size for selective oxidation in the presence of $H_2$

53

The data shown in Table 3.6 shows that increasing the calcination temperature increases the mean particle size of the gold and the oxide support. This effect is to be expected since the higher temperature increases the atomic mobility so that significant sintering occurs.

This increasing particle size has the effect of reducing the ability of the catalyst to oxidize CO, as evidenced by the plot in Figure 17. Clearly, as the Au particle size increases the amount of CO converted progressively decreases, and finally reaches zero for the catalyst calcined at 600 °C.

This particle size-activity correlation is in keeping with the early findings of Haruta and those reported by more recent researchers, in that the catalytic activity decreases when the particle size begins to exceed the 2-5 nm range and continues to decrease as the particles grow ever larger [6].

The only sample that exhibits a strong tendency towards hydrogen oxidation is 25.1, which was dried at 120 °C. Since there is very little difference in gold particle size between 25.1 and 25.2, it appears that a further critical component for hydrogen oxidation is the size and structure of the oxide support.

As with the dried samples examined in the previous section, sample 25.1 contains extremely small haematite particles as well as the layered morphology typical of goethite. Therefore, it appears that the reduced size of the haematite particles or the presence of the goethite structure encourages the oxidation of the hydrogen molecules. Figure 18 shows the drastic difference between the dried sample and the sample calcined at 600 °C, while Figure 19 reveals the very small gold particles in the dried sample (25.1) at high magnification.

**Figure 18** – Bright-field TEM images of Au/Iron oxide for CO oxidation in the presence of $H_2$, [300kX] Sample 25.1 dried at 120 °C (left) and Sample 25.5 calcined at 600 °C (right)



**Figure 19** – High resolution image of sample 25.1 dried at 120 °C revealing 1 nm Au particles. [1 MX]
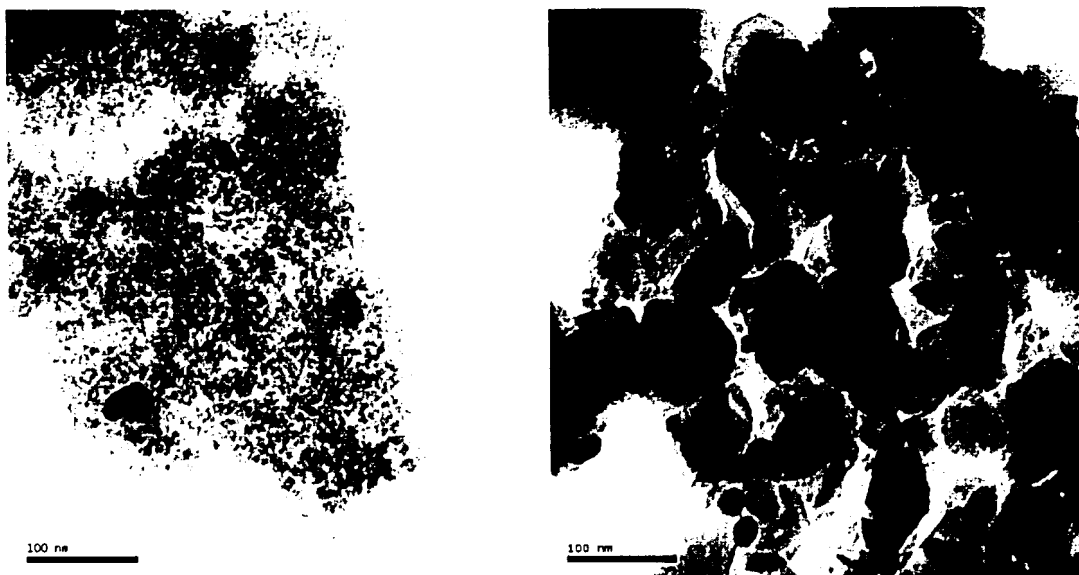
**Figure 18** – Bright-field TEM images of Au/Iron oxide for CO oxidation in the presence of $H_2$, [300kX] Sample 25.1 dried at 120 °C (left) and Sample 25.5 calcined at 600 °C (right)
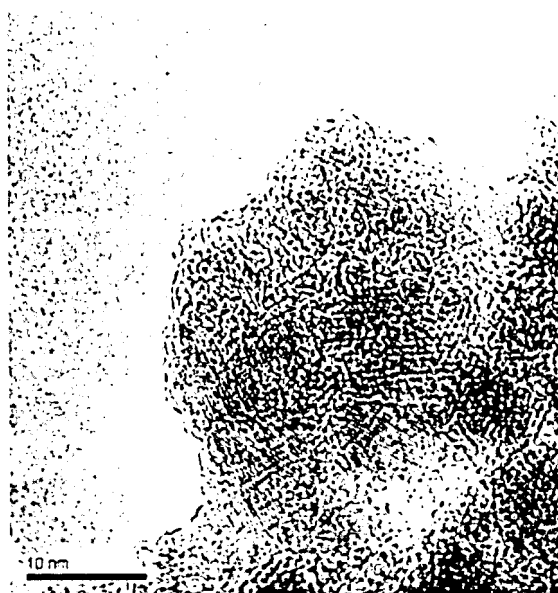


**Figure 19** - High resolution image of sample 25.1 dried at 120 °C revealing 1 nm Au particles, [1 MX]
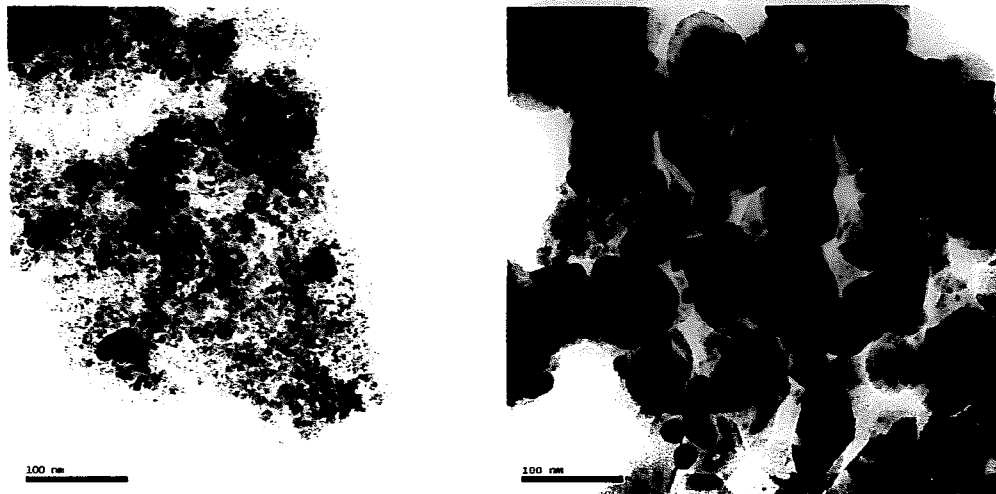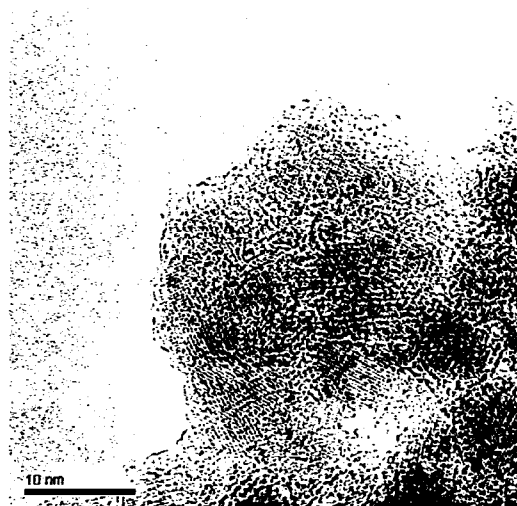
### 3.2.3 Summary of Au/Iron Oxide for Selective CO Oxidation in the Presence of $H_2$

Therefore, the selective oxidation of CO in the presence of hydrogen depends upon the calcination treatment used in producing the catalyst. Using an elevated heat treatment increases the gold and oxide particle sizes and promotes the conversion of goethite particles to haematite. Both of these effects were shown previously to reduce the activity of the catalyst for CO oxidation, but now they have also been found to reduce the activity for hydrogen oxidation to zero.

These findings are remarkable in that previous research on other oxide supported gold catalysts, such as $Au/CeO_2$, has shown that the selectivity completely breaks down as the reaction temperature is increased [35]. The combination of high CO conversion and very low $H_2$ conversion over a temperature range of nearly 50 °C makes this system an extremely promising catalyst for several future applications, especially that of on-stream $H_2$ purification for fuel cells.

### 3.3 Au/Zinc Oxide for Methane Oxidation

In this section, the goal will be to understand the way in which the addition of gold to zinc oxide improves its catalytic performance for partial oxidation of methane. Microstructural data will be presented and interpreted in the section 3.3.2 with the intention of explaining the catalytic results presented section 3.3.1.

### 3.3.1 Catalytic Testing Results

The catalytic testing results for the Au/Zinc oxide catalysts presented in Table 3.7 show that the addition of gold to zinc oxide has a strong effect on two measures of its

catalytic activity: lightoff temperature and activation energy. Considering only samples

Z0 – Z5 (the uncalcined group), we see that the addition of 1 at.% gold reduces both the

light-off temperature and the activation energy. In other words, it improves the activity

of the catalyst and reduces the temperature at which it becomes operable. Similarly,

when 2 at.% gold (Z2) is added the light-off temperature and activation energy are further

reduced.

Table 3.7 - Catalytic testing results of Au/Zinc oxide samples for methane oxidation

| Sample ID | Gold Content (at. %) | Activation Energy (kJ/mol) | Pre-exponential Function | Lightoff Temperature (K) |
|---|---|---|---|---|
| Z0 | 0 | 118 | 56.98 | 623 |
| Z1 | 1 | 97 | 55.21 | 548 |
| Z2 | 2 | 76 | 52.07 | 508 |
| Z5 | 5 | 97 | 54.46 | 543 |
| ZC0 | 0 | 113 | 56.40 | 593 |
| ZC1 | 1 | 110 | 57.36 | 578 |

However, the addition of 5 at.% gold (Z5) causes both of these variables to return to a

value that is comparable to that of the sample containing only 1 at.% gold (Z1). Finally,

adding 1 at.% gold to the calcined zinc oxide (ZC1) again reduces both the light-off

temperature and the activation energy, however, not to the same degree exhibited in the

corresponding uncalcined catalyst.

### 3.3.2 Electron Microscopy Results

The SAD patterns shown in Figure 20 show that whether calcined or uncalcined,

the support particles exhibited the ZnO wurtzite structure, shown schematically in

Figure 21. Refer to Appendix B for the observed and theoretical indexing ratios. This is

confirmed by the HRTEM lattice image in Figure 22 where the plane spacings are

directly indexed to the ZnO structure. The formation of ZnO is somewhat



Figure 20 - SADP patterns of calcined ZnO (left) and uncalcined ZnO with 5%Au



Figure 21 – Schematic diagram of ZnO wurtzite structure, oxygen = red and zinc = gray

unexpected since the anticipated morphology of hydrozincite ($Zn_5(CO_3)_2(OH)_6$) only

decomposes at 245 °C [36] and previous studies [37] had reported that the formation of

58

confirmed by the HRTEM lattice image in Figure 22 where the plane spacings are

directly indexed to the ZnO structure. The formation of ZnO is somewhat
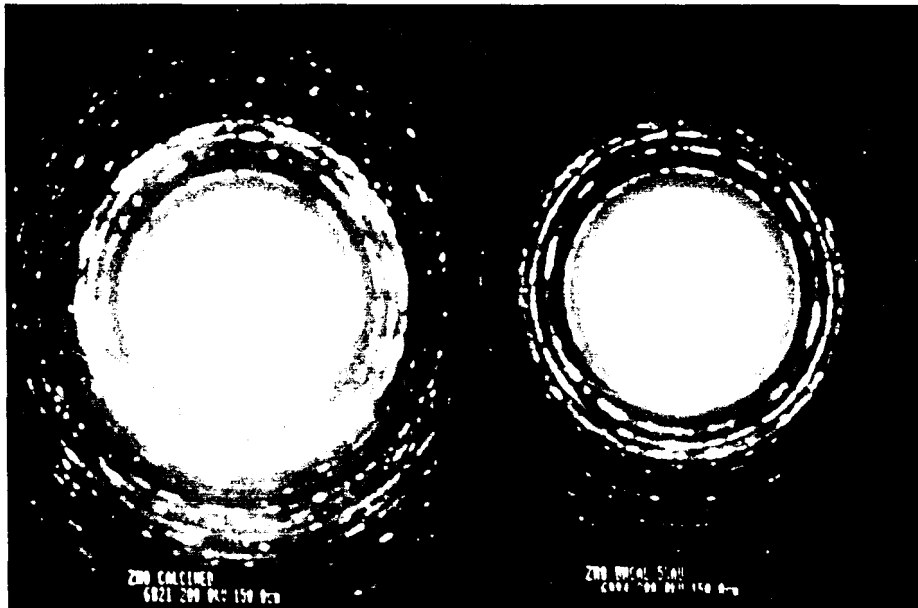


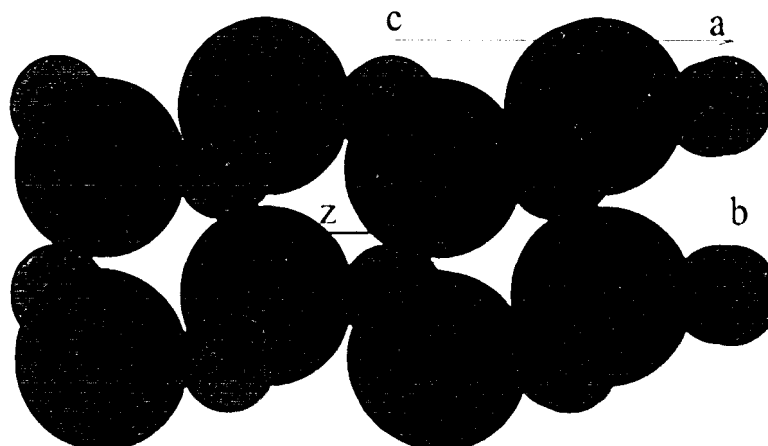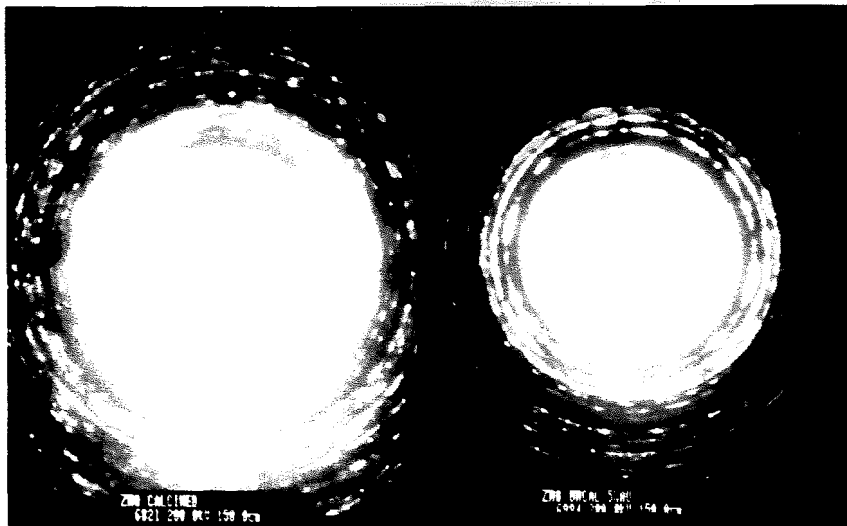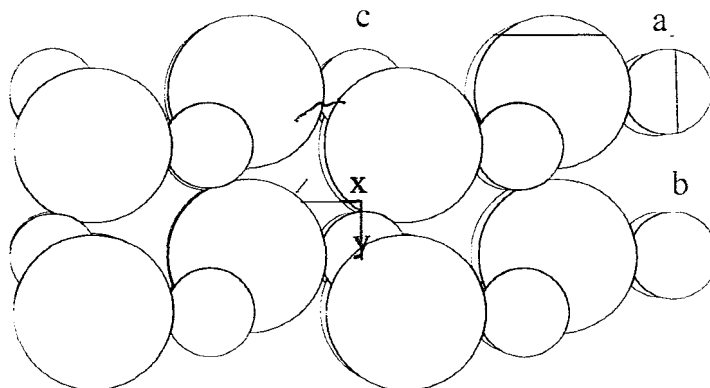**Figure 20** - SADP patterns of calcined ZnO (left) and uncalcined ZnO with 5%Au



**Figure 21** – Schematic diagram of ZnO wurtzite structure. oxygen – red and zinc – gray

unexpected since the anticipated morphology of hydrozincite $(Zn_5(CO_3)_2(OH)_6)$ only

decomposes at 245 °C **[36]** and previous studies **[37]** had reported that the formation of

ZnO only occurred after calcination above 240 °C. However, it was also reported that hydrozincite supported gold was a poor catalyst so the formation of the wurtzite structure is beneficial though unexpected.



Figure 22 - HRTEM lattice image of ZnO catalyt showing [110] plane spacings (0.17 nm) [3 MX]

The representative bright field TEM images presented in Figure 23 show that adding 2 at.% gold to the uncalcined zinc oxide sample reduces the oxide particle size by 61 %, from 146 to 57 nm. Adding 1 at.% gold has a lesser but similar effect. The further addition of 5 at.% gold causes the oxide particle size to increase to 176 nm, exceeding even that of the pure uncalcined zinc oxide. A similar trend is observed in the set of calcined samples, where the oxide particle size is reduced from 168 to 82 nm by the addition of 1 at.% Au. In contrast to this, the mean gold particle size observed remains approximately constant from one uncalcined sample to the next. However, there are more particles apparent in the 5 at.% Au sample than there are for the others.

A representative HAADF image of sample Z2 is shown in Figure 24 and shows the Au particles to be approximately 2 nm in size. The calcined Au particles in sample ZC1 are much larger (approximately 8 nm) due to sintering at the elevated temperature. Particle size data for all samples in this set are collected in Table 3.8.
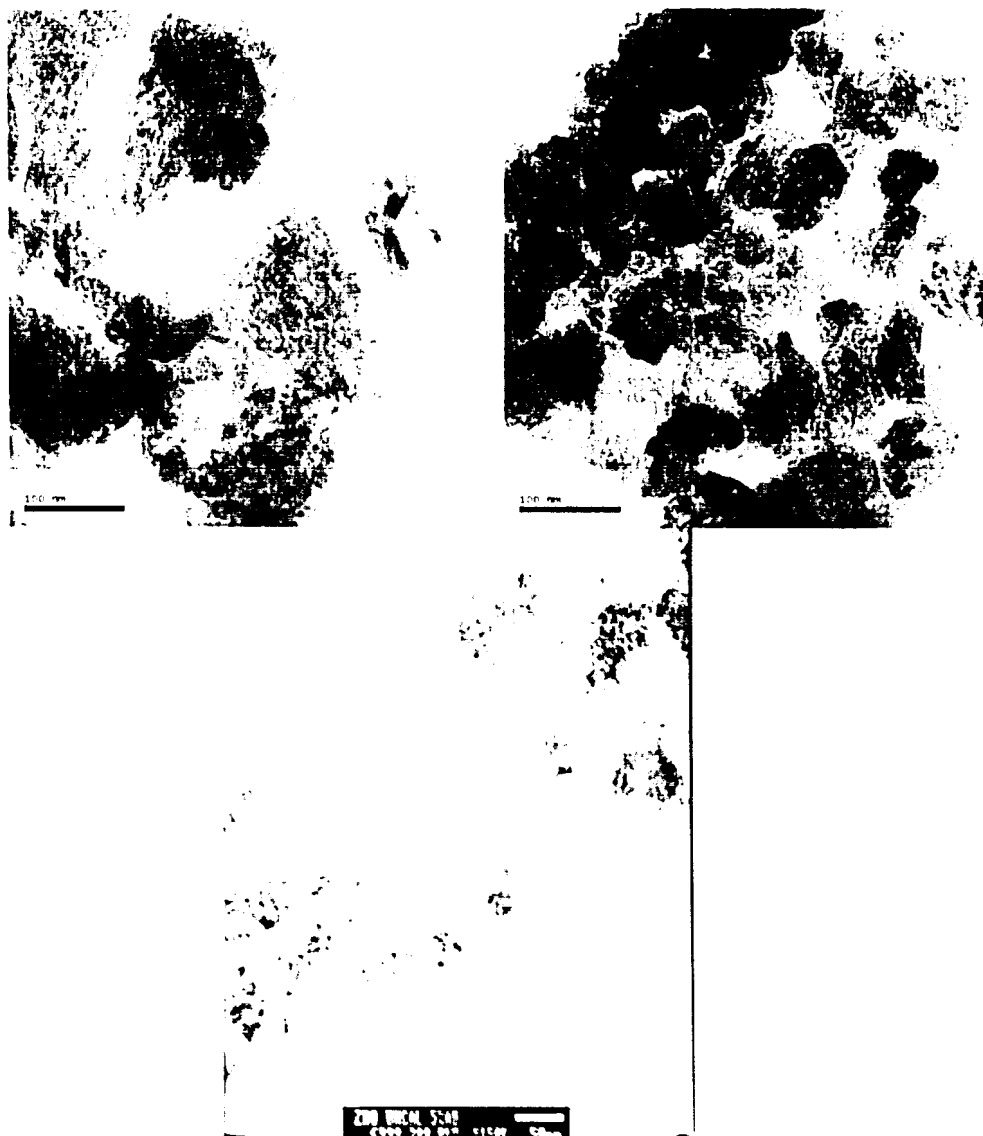


Figure 23 – Bright field TEM images of sample Z0 uncalcined ZnO [left, 300kX], Z2 uncalcined ZnO – 2 at.% Au [right, 300kX], and Z5 uncalcined ZnO – 5 at.% Au [bottom, 150kX]

**Figure 24** - HAADF image of small Au particles in sample Z2, [1 MX]

If these particle sizes are correlated with the catalytic testing results, it can be seen that the trend followed by the light-off temperature and activation energies is mirrored by the oxide particle size. That is, the addition of gold improves the catalytic performance and reduces the oxide particle size until a minimum is reached at 2 at.% gold. Further addition of gold becomes detrimental to catalytic performance and increases the oxide particle size.

Therefore, it appears that the gold particles are in some way stabilizing smaller zinc oxide support particles. This effect reaches a maximum near 2 at.% Au whereupon the addition of further gold appears to be less effective and the particles stabilized are larger.

Table 3.8 - Particle size data for Au/Zinc oxide catalysts for methane oxidation

| Sample ID | Au Particle Size (nm) | Oxide Particle Size (nm) |
|-----------|----------------------|--------------------------|
| Z0 | - | 146 |
| Z1 | 2.4 | 88 |
| Z2 | 2.1 | 57 |
| Z5 | 2.0 | 176 |
| ZC0 | - | 168 |
| ZC1 | 8.1 | 82 |

* - Averaged over twenty particle size measurements

Pennycook et al observed a similar phenomenon in lanthanum-doped alumina samples [38]. The transformation of the catalytically active porous $\gamma$-$Al_2O_3$, which typically transforms to inactive, non-porous $\alpha$-$Al_2O_3$ at 1100 °C, is raised to 1250 °C when doped with lanthanum. It was found using aberration corrected TEM that the presence of single atoms and small clusters of lanthanum prevented the sintering of the alumina particles by a strong mutual repulsion. An image gathered during their work is presented below in Figure 25, showing the remarkable power of aberration corrected microscopy techniques. In the image, the very bright spots superimposed on the square Al-O lattice represent lanthanum atoms.

A similar phenomenon could be occurring in the Au/Zinc oxide system, in that the presence of small gold clusters inhibit the growth of the oxide particles. This inhibition increases the effective surface area of the catalyst and improves its catalytic performance. However, the reason that the addition of gold in excess of 2 at.% fails to bring about the same behavior is less clear. It may be that the single gold atoms necessary to prevent

growth show a greater tendency to cluster into larger metal particles as evidenced by the

images in Figure 23.
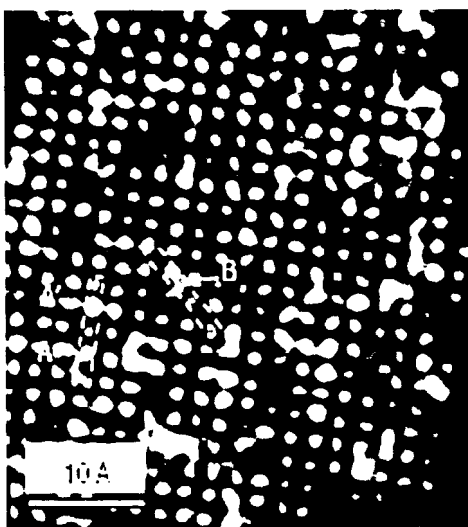


**Figure 25** - Aberration corrected HAADF image of single La atoms adsorbed onto alumina catalyst in two distinct lattice positions A(A') and B [38]

### 3.3.3 Summary of Au/Zinc Oxide for Methane Conversion

The lightoff temperature of the ZnO catalysts reduced significantly with the

addition of 1 at.%Au. A further decrease in the lightoff temperature was observed with

the addition of 2 at.% Au, but the addition of 5 at.% Au actually caused the lightoff

temperature to increase.

A parallel trend was observed in the oxide particle size variation with increasing

gold content, indicating a possible correlation between catalytic activity and ZnO particle

size. A similar effect was reported in alumina catalysts doped with lanthanum, where

single lanthanum atoms dispersed on the oxide surface inhibited densification and phase

transformation thereby improving the catalyst stability. It is possible that individual gold

atoms or clusters that are too small to be imaged with conventional TEM techniques are having the same effect on the ZnO particles, and it is the presence of these highly dispersed species that improves the catalytic performance. However, the reason that adding 5 at.%Au does not further improve this effect is unknown at the present time. It may be that more of the gold atoms take part in the formation of larger particles and are therefore no longer dispersed as single atoms or small clusters and their growth inhibiting character is thus lost.

## 3.4 Au-Pd Bimetallic Catalysts for $H_2O_2$ Production

The following is an overview of the findings regarding the Au-Pd catalysts which were studied for their ability to produce hydrogen peroxide by direct combination of hydrogen and oxygen. Specifically, the focus of this section is to illuminate the nature of the metallic particles (composition, structure, size, etc.) and the various oxide supports used. Previous sections have shown that these factors are critical to the process of CO oxidation and methane conversion, so it is reasonable to assume that structural properties of the bi-metallic catalyst will influence their performance.

### 3.4.1 Catalytic Testing Results

The results of catalytic testing of the Au-Pd bimetallic specimens for $H_2O_2$ production are summarized in Table 3.9 and show several interesting traits. First, it can be seen that regardless of the support used (i.e. $Al_2O_3$, $Fe_2O_3$, or $TiO_2$) the pure gold samples are extremely poor catalysts. In contrast, the pure palladium samples show some

limited ability to catalyze the direct combination reaction, although it is still so slight as to be commercially impractical.

However, when gold and palladium are used in combination with each other, there is a significant improvement in the catalytic performance of all the oxide supports. This remains true whether a small amount of gold is added to palladium, or whether a small amount of palladium is added to gold. These results are also shown graphically in Figure 26.

**Table 3.9 - Catalytic testing results of Au-Pd catalysts for $H_2O_2$ production**

| Sample ID Titania | Productivity mol/h/Kg$_{cat}$ | Sample ID Alumina | Productivity mol/h/Kg$_{cat}$ | Sample ID Haematite | Productivity mol/h/Kg$_{cat}$ |
|---|---|---|---|---|---|
| APT1 (5%Au) | 7 | APA1 (5%Au) | 2.5 | APF1 (5%Au) | 0.5 |
| APT2 (4%Au–1%Pd) | 28 | APA2 (2.5%Au-2.5%Pd) | 18 | APF2 (2.5%Au-2.5%Pd) | 15 |
| APT3 (2.5%Au-2.5%Pd) | 56 | APA3 (5%Pd) | 15 | APF3 (5%Pd) | 4 |
| APT4 (5%Pd) | 30 | APA4 (Uncal. APA2) | 9 | | |
| APT5 (2.5%Au-2.5%Pd) Uncalcined | 202 | | | | |

The ratio of gold to palladium also appears to be critical to maximizing the peroxide production capability of the catalyst. It can be readily seen that for each support, the catalytic performance reaches its peak *for* the sample containing 2.5 at.% Au and 2.5 at.% Pd. This is especially true for the titania system where this combination of

gold and palladium shows an $H_2O_2$ productivity of 56 and 202 mol/h/Kg$_{cat}$ for the calcined and uncalcined catalysts respectively.

Therefore, it seems that a synergistic effect is produced by combining gold and palladium, and that this effect occurs regardless of which oxide support is chosen (although the effect is more dramatic in the titania system). Furthermore, the catalytic activity is maximized by having a Au:Pd ratio of 1:1.
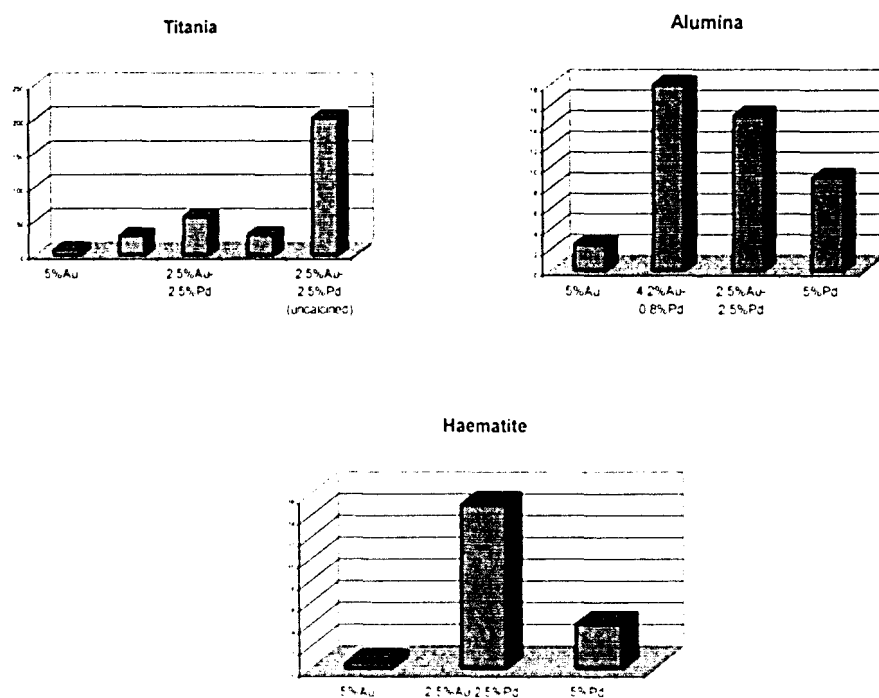


Figure 26 – Graphical representation of productivity of each grouping of Au-Pd catalysts

### 3.4.2 XPS Results

The XPS results for these bi-metallic catalysts, shown in Figure 27, reveal an interesting phenomenon. While the spectrum for the uncalcined sample at the bottom shows the clear presence of gold and palladium, the Au(4d) signal disappears after calcination at 200 °C and remains hidden after further calcination at 400 °C and reduction at 500 °C. This suggests that homogenous alloys form after catalyst synthesis, but that the subsequent heat treatment causes the gold to disappear from the surface sensitive XPS analysis zone. One possible explanation is that the gold diffuses into the oxide support. Another, much more likely scenario is that the palladium atoms migrate to the surface of the bi-metallic particle during calcination.
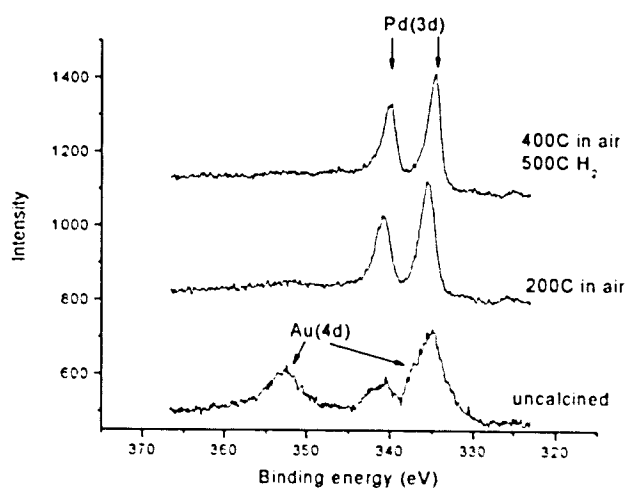


Figure 27 - XPS Results for 2.5%Au-2.5%Pd $Fe_2O_3$ sample showing possible surface segregation of palladium atoms

Since the photoelectrons created in the XPS process have such a low energy, they are not able to travel through a great distance of the material without being absorbed. Because of this, only those electrons produced near the surface are collected and the resulting composition calculations are only relevant for the material within a few atomic layers of the surface. Therefore, the two scenarios mentioned above could account for the lack of gold signal present in the XPS results after calcination.

This behavior seems to contradict the complete solid solution predicted by the thermodynamic phase diagram shown in Figure 28 [39], but there is some reason to expect this phase segregation effect since similar behavior in bulk Au-Pd alloys has been reported [40].

The reason for this is that palladium oxidizes much more readily at the calcination temperature (400 °C) than gold, which only begins to oxidize near 700 °C. Because of this, the palladium atoms may preferentially migrate to the surface to form Pd-O bonds. It was also reported [40] that when the bulk alloy was subsequently reduced in a hydrogen atmosphere, as the catalysts in question were, the Pd-O bonds were destroyed but the palladium surface enrichment was retained. Therefore, a similar phenomenon could very well be occurring in these bi-metallic nanoparticles on a much smaller scale.
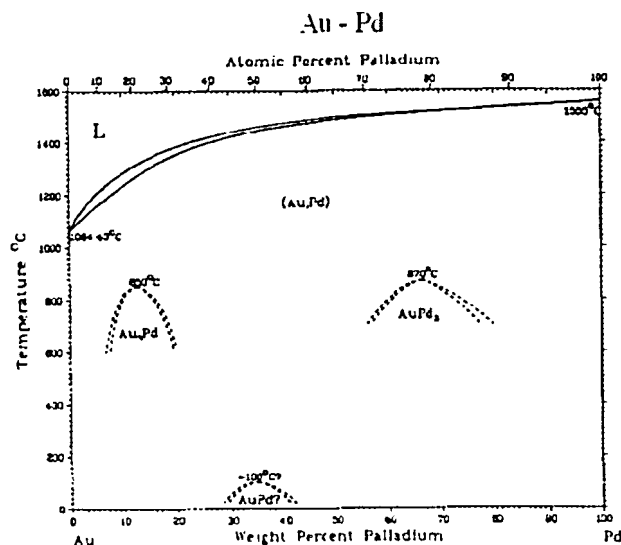
**Figure 28** - Equilibrium phase diagram for the Au-Pd system showing complete solid solution behavior[36]

If segregation is present, it could be responsible for the synergistic increase in catalytic activity exhibited by the bi-metallic samples relative to the pure gold and pure palladium samples. Such segregation would produce a dilute gold solution in a palladium matrix, with a consequential alteration of the electronic structure of the gold atoms. Weinberger and Szunyogh [41] showed that the Au-5d$^{3/2}$ density of states changed significantly as the coordination of palladium atoms surrounding it increased. Similar measurements showed an even more dramatic change in the Pd-4d$^{3/2}$ density of states when it was surrounded by an increasing number of gold atoms. Changes are also seen in the binding energies of these two electron bands with increasing gold contents with the Au-5d$^{3/2}$ binding energy decreasing and the Pd-4d$^{3/2}$ binding energy increasing linearly. These findings from Weinberger are shown graphically below in Figure 29.

Therefore, since the electronic structure of the gold and palladium atoms is altered by increasing the coordination of one around the other, it may be that this electronic process is responsible for the increase in catalytic activity.
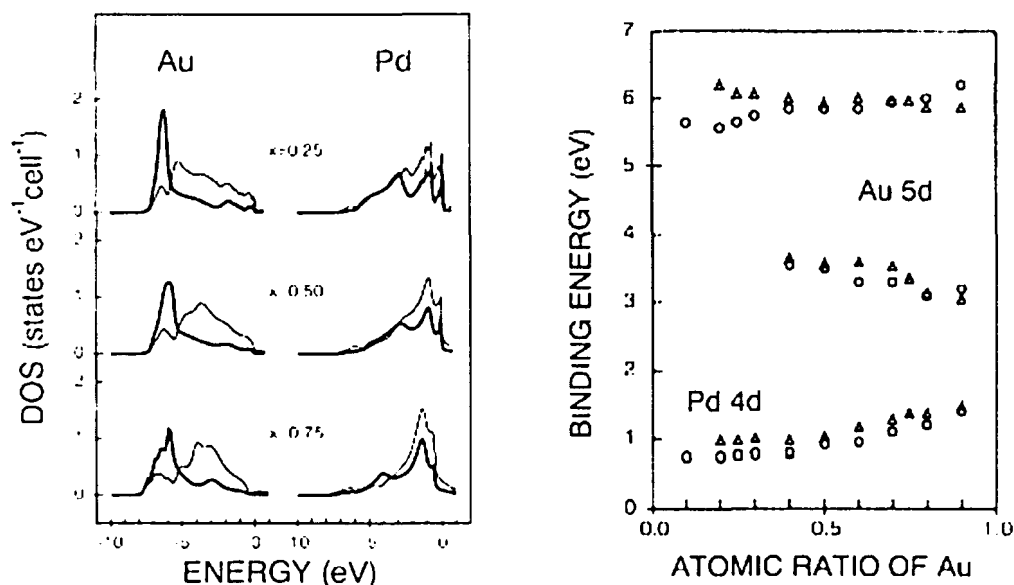


Figure 29 – Density of states (left) and binding energies for Au and Pd d electrons in Au$_x$Pd$_{1-x}$; thick lines represent the d$_{3/2}$ electron and thin lines represent the d$_{5/2}$ electrons [41]

### 3.4.3 Electron Microscopy Results

Particle size measurements derived from HAADF imaging experiments for the bimetallic catalysts are shown in Table 3.10. The initial HAADF images shown in Figure 30 of the bi-metallic catalysts revealed a bi-modal particle size distribution with very small particles (<5nm) and also very large metal particles the majority of which were in the 30 – 70 nm range with some even exceeding 120 nm in size. This is in stark contrast to all of the previous catalysts examined, which tended to contain particles of 10 nm or less. Also shown in Figure 30 are Au, Pd, O, and Fe XEDS maps revealing that the metal particles are alloys of gold and palladium rather than either pure gold or pure palladium particles.

Table 3.10 – Particle size data for Au-Pd bi-metallic catalysts for $H_2O_2$ production

| Sample ID | Description | Small Metal Particle Size (nm) | Large Metal Particle Size (nm) |
|---|---|---|---|
| APA2 | 2.5%Au-2.5%Pd / $Al_2O_3$ | 3.6 | 38 |
| APF1 | 5%Au / $Fe_2O_3$ | - | 48 |
| APF2 | 2.5%Au-2.5%Pd / $Fe_2O_3$ | 4.6 | 32 |
| APF3 | 5%Pd / $Fe_2O_3$ | - | 53 |
| APT2 | 4%Au-1%Pd / $TiO_2$ | - | 52 |
| APT3 | 2.5%Au-2.5%Pd / $TiO_2$ | 2.1 | 48 |
| APT5 Uncalcined | 2.5%Au-2.5%Pd / $TiO_2$ | 1.4 | 46 |

\* - Averaged over twenty particle size measurements

Another feature of the EDS maps is that the palladium signal appears to be coming from

a larger spatial area than the gold signal. This finding at first sight seemed to confirm the

results of the complimentary XPS study that suggested palladium surface segregation.

However, the short dwell time of 100 µs used to limit the effects of beam damage

produced only 6-10 Pd counts per pixel at most. While there were over 40 Au counts per

pixel, the low number of Pd counts creates a very large error since statistics dictate that

the proximity of a sampled population to the actual population varies inversely with $N^{1/2}$,

where N is the number of samplings. The increased number of Au counts can be

dependent on beam energy and incident angle, is proportional to $Z^2$ [17]. Therefore, the

cross-section of the gold atom (Z = 79) is much larger than that of palladium (Z = 46).

explained because the Rutherford scattering cross-section, while highly

**Figure 30 –** HAADF image (top) and corresponding XEDS maps of Pd (upper right), Au (upper left), Fe (lower left) and O (lower right) signals in 2.5%Au-2.5%Pd/$Fe_2O_3$ sample (APF2) . [100 μs Dwell Time]

In an attempt to correct for this, the raw XEDS data was statistically analyzed using a multivariate statistical analysis (MSA) program. This statistical technique performs a data smoothing calculation by partitioning the EDS data into 'likely' regions and using a probability density function to reduce statistically unlikely data points [42].
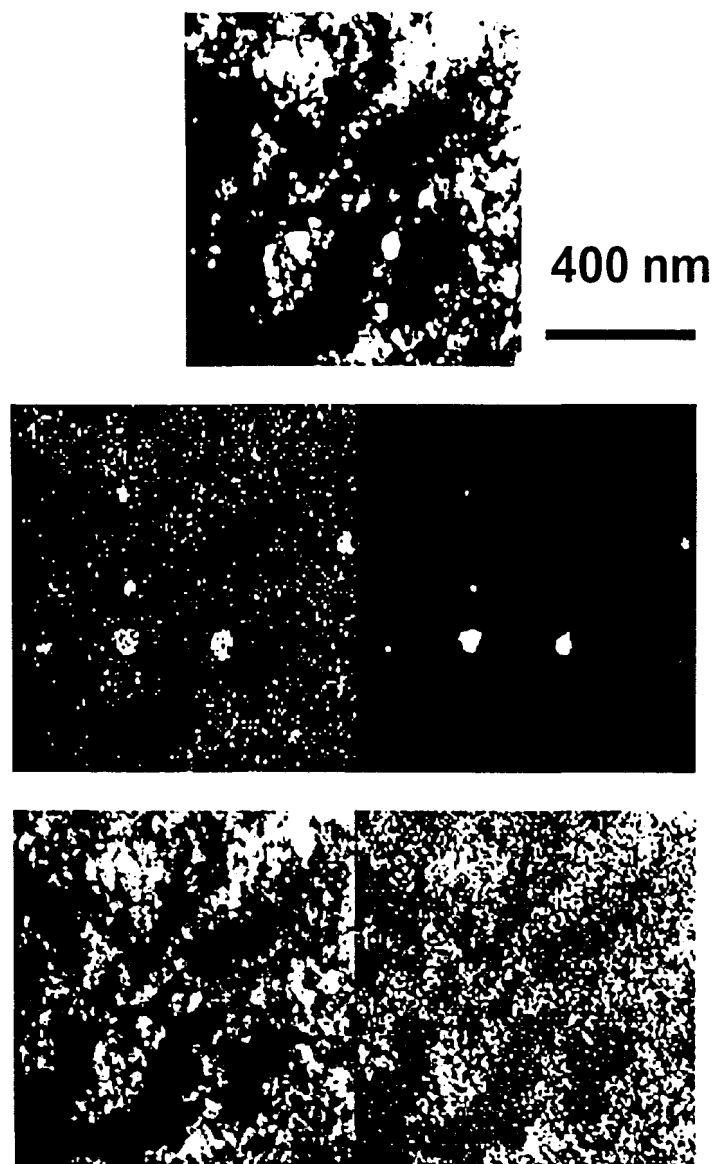
**Figure 30** – HAADF image (top) and corresponding XEDS maps of Pd (upper right), Au (upper left), Fe (lower left) and O (lower right) signals in 2.5%Au-2.5%Pd/Fe$_2$O$_3$ sample (APF2) , [100 μs Dwell Time]

In an attempt to correct for this, the raw XEDS data was statistically analyzed using a multivariate statistical analysis (MSA) program. This statistical technique performs a data smoothing calculation by partitioning the EDS data into 'likely' regions and using a probability density function to reduce statistically unlikely data points [42].

This allowed the maps to more accurately reflect the area producing the X-ray signals. When the previous map is observed following the MSA filtering, the result is shown in Figure 31.



Figure 31 - HAADF image (top) and MSA corrected XEDS maps of Pd (upper left), Au (upper right), Fe (lower left) and O (lower right) signals in 2.5%Au-2.5%Pd Fe₂O₃ sample (APF2). [100 μs Dwell Time]

This allowed the maps to more accurately reflect the area producing the X-ray signals. When the previous map is observed following the MSA filtering, the result is shown in Figure 31.
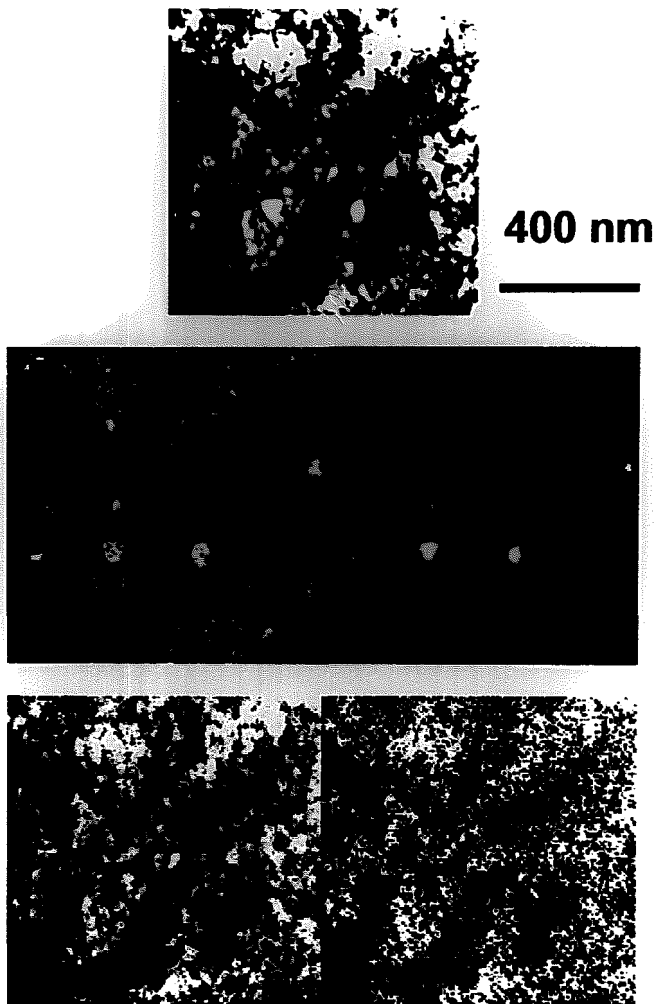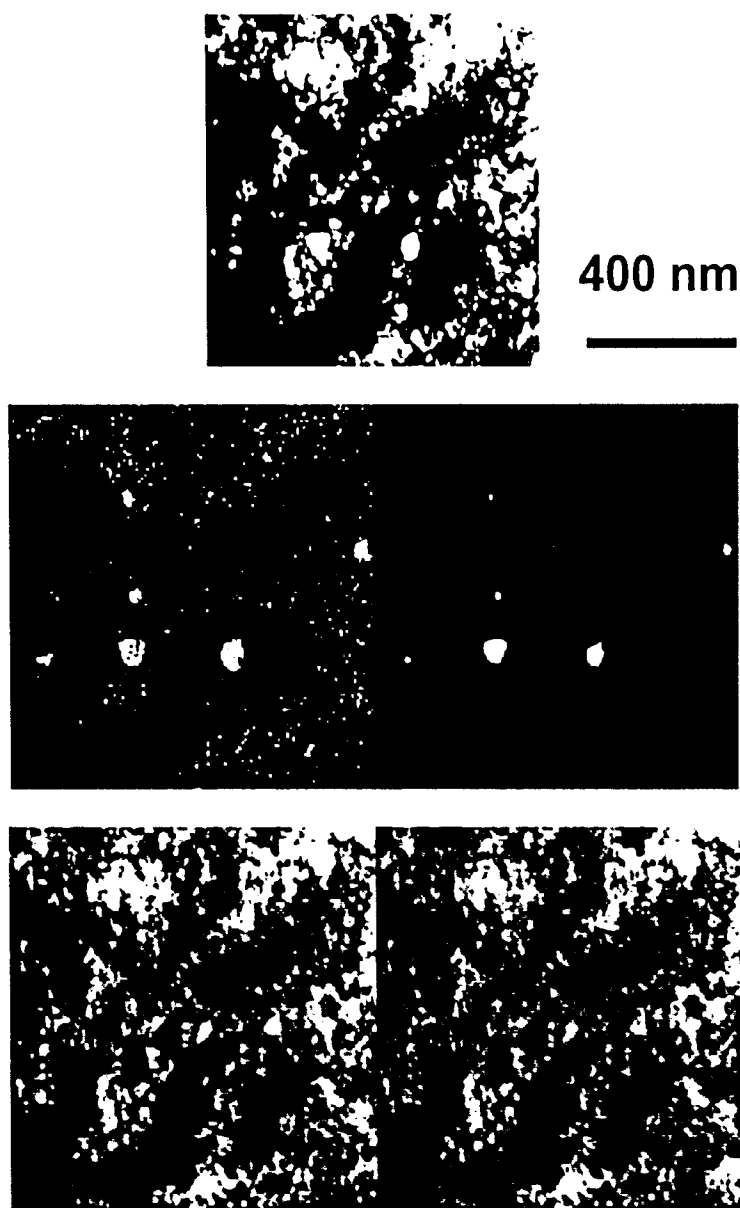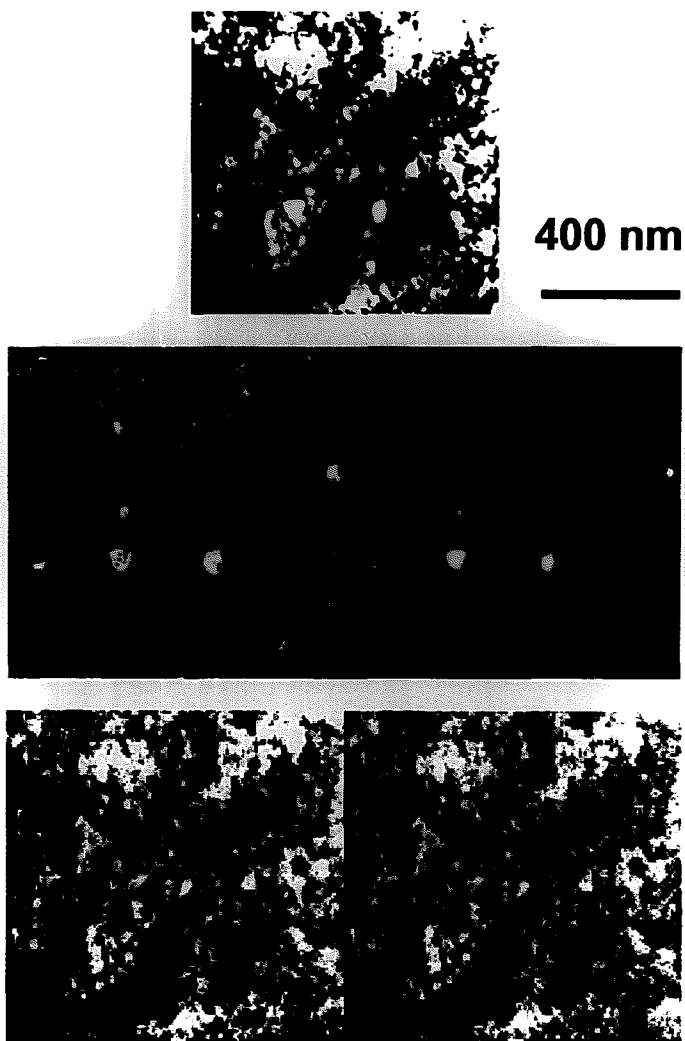


**Figure 31** - HAADF image (top) and MSA corrected XEDS maps of Pd (upper left), Au (upper right), Fe (lower left) and O (lower right) signals in 2.5%Au-2.5%Pd/Fe$_2$O$_3$ sample (APF2), [100 μs Dwell Time]

In this set of images, while the noise is substantially reduced by the MSA analysis, the palladium signal still appears to be coming from a larger area than that of the gold signal.

Another perspective of this is shown in Figure 32, where the Pd signal has been fully isolated from the gold signal and noise. Here, it is clearly evident that the palladium is most prominent in the perimeter of the particle. Reconstructing the image using a red (oxygen), green (gold), and blue (palladium) scheme, the result clearly shows the formation of a palladium shell with a gold core.



**400 nm**

Figure 32 - HAADF image (left) of 2.5 -Au-2.5 -Pd Fe$_2$O$_3$ sample with a fully isolated palladium map (center) and reconstructed RGB image: red = oxygen, green = gold, and blue = palladium

In this set of images, while the noise is substantially reduced by the MSA analysis, the palladium signal still appears to be coming from a larger area than that of the gold signal.

Another perspective of this is shown in Figure 32, where the Pd signal has been fully isolated from the gold signal and noise. Here, it is clearly evident that the palladium is most prominent in the perimeter of the particle. Reconstructing the image using a red (oxygen), green (gold), and blue (palladium) scheme, the result clearly shows the formation of a palladium shell with a gold core.
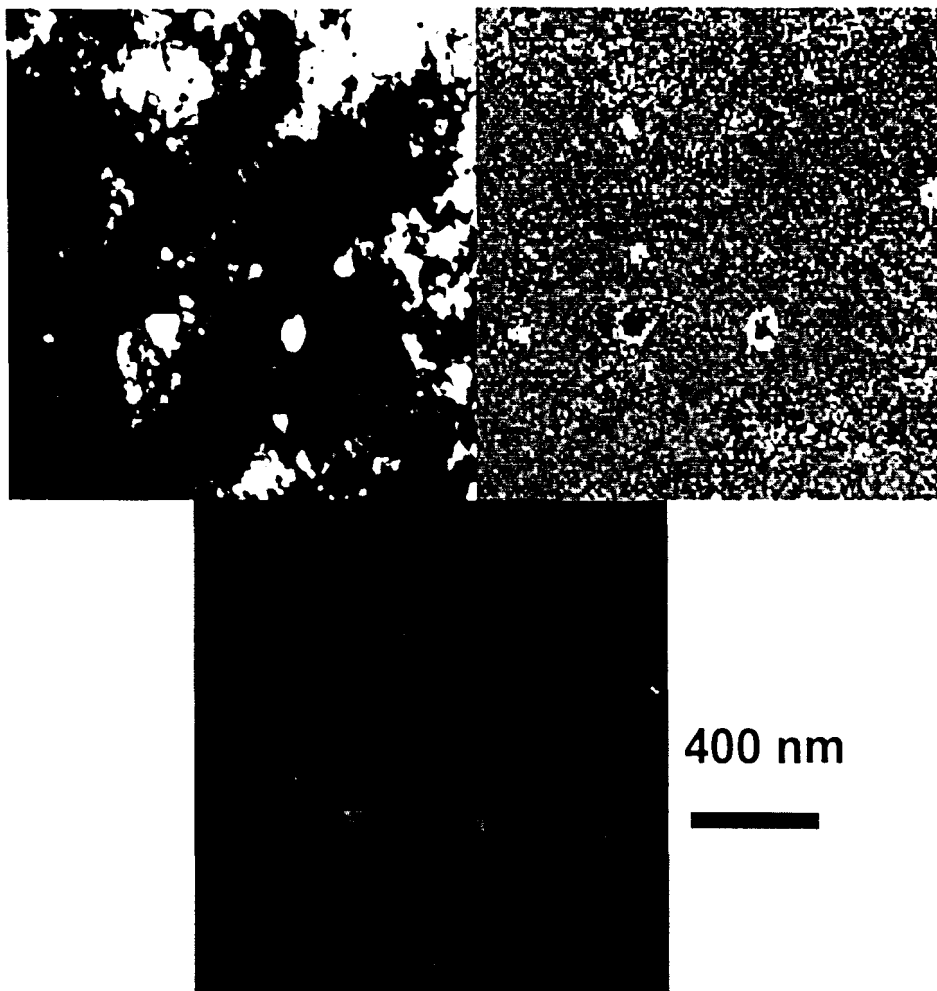


**Figure 32** - HAADF image (left) of 2.5%Au-2.5%Pd/Fe$_2$O$_3$ sample with a fully isolated palladium map (center) and reconstructed RGB image: red = oxygen, green = gold, and blue = palladium

Further evidence of a core-shell structure is shown in Figure 33. The HRTEM image of a single alloy particle from sample APF2 reveals a continuous pattern of lattice fringes from the interior of the particle to the perimeter. If there were a shell of palladium oxide surrounding the particle, the large difference in lattice parameters would produce a Moire fringe pattern. Therefore, if the core-shell structure does exist then it is a metal-metal structure since gold and palladium have similar lattice parameters and would produce no such Moire effect. However, there does appear to be a very slight, abrupt change in contrast between a darker circular region in the center and the lighter region of the perimeter. This sort of circular core could also indicate a difference in composition between the interior and perimeter, since a contrast change caused by thickness variation in a hemispherical particle would have been more gradual.



Figure 33 - HRTEM image of sample APF2 showing a single Au-Pd particle and a possible core-shell structure. [2 0 0] Zone axis, plane spacings approximately 2 Angstroms. [800 kX]

A further indication of surface segregation in the metal particles is shown in

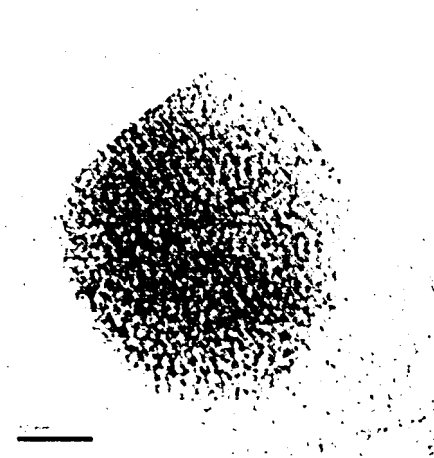Figure 34. A line scan across an XEDS map taken with a 200 μs dwell time shows a

clear difference in count distribution. The gold signal follows a Gaussian distribution

with a maximum at the particle center, while the palladium signal shows a "top-hat"

distribution where the counts are relatively flat across the particle but with slight peaks

near the perimeter.



40 nm                          40 nm

**Figure 34** - Line scan of XEDS map data for sample APA2 Au $M_2$ (left) and Pd $L_1$ (right) showing difference in count distribution. [200 μs dwell time]

The extent of segregation can be numerically estimated if the extreme case is

considered where 100% of the palladium forms an outer-shell around a 100% gold core.

In this case, the thickness of the shell layer in a 40 nm particle will be only 12 nm. The

result is a core to particle radius of 0.8. This simple calculation is illustrated graphically

in Appendix C. If a similar calculation is performed for the HRTEM image in Figure 33,

the radius of the core is found to be approximately 13.5 nm in diameter while the radius

of the entire particle is approximately 17 nm. Therefore, the ratio of the core radius to

the radius of the whole particle is 0.8, the identical value calculated in the theoretical

A further indication of surface segregation in the metal particles is shown in Figure 34. A line scan across an XEDS map taken with a 200 μs dwell time shows a clear difference in count distribution. The gold signal follows a Gaussian distribution with a maximum at the particle center, while the palladium signal shows a "top-hat" distribution where the counts are relatively flat across the particle but with slight peaks near the perimeter.
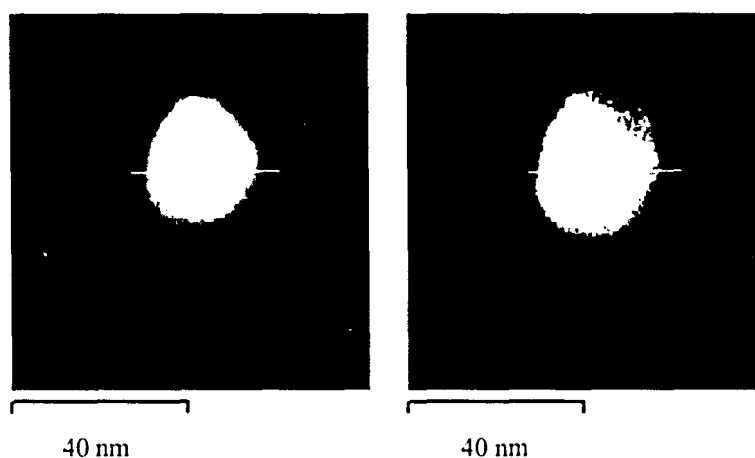


40 nm          40 nm

**Figure 34** - Line scan of XEDS map data for sample APA2 Au $M_2$ (left) and Pd $L_1$ (right) showing difference in count distribution, [200 μs dwell time]

The extent of segregation can be numerically estimated if the extreme case is considered where 100% of the palladium forms an outer-shell around a 100% gold core. In this case, the thickness of the shell layer in a 40 nm particle will be only 12 nm. The result is a core to particle radius of 0.8. This simple calculation is illustrated graphically in Appendix C. If a similar calculation is performed for the HRTEM image in Figure 33, the radius of the core is found to be approximately 13.5 nm in diameter while the radius of the entire particle is approximately 17 nm. Therefore, the ratio of the core radius to the radius of the whole particle is 0.8, the identical value calculated in the theoretical

76

model above  Similar values can be obtained if the image in Figure 32 is analyzed like this.

Similar core-shell structures in nanoparticles have been found in the Au-Ag system [43].  Since the Au-Ag phase diagram also predicts a complete solid solution, this is further evidence to support the possibility of a surface-rich palladium layer in these catalysts.

Although the particles discussed thus far have been extremely large when compared to the previous catalysts, the bi-metallic samples also contained extremely small particles that were approximately 1 nm in size.  In order to resolve them, the signal gain was increased on the STEM so that the larger particles were washed out with brightness, but in so doing the smaller particles were rendered more visible.  Examples of this are shown in Figure 35 for sample APT3.  The particle sizes for all of the supports were fairly similar so it would seem that the active sites for the reaction are the same regardless of support used.
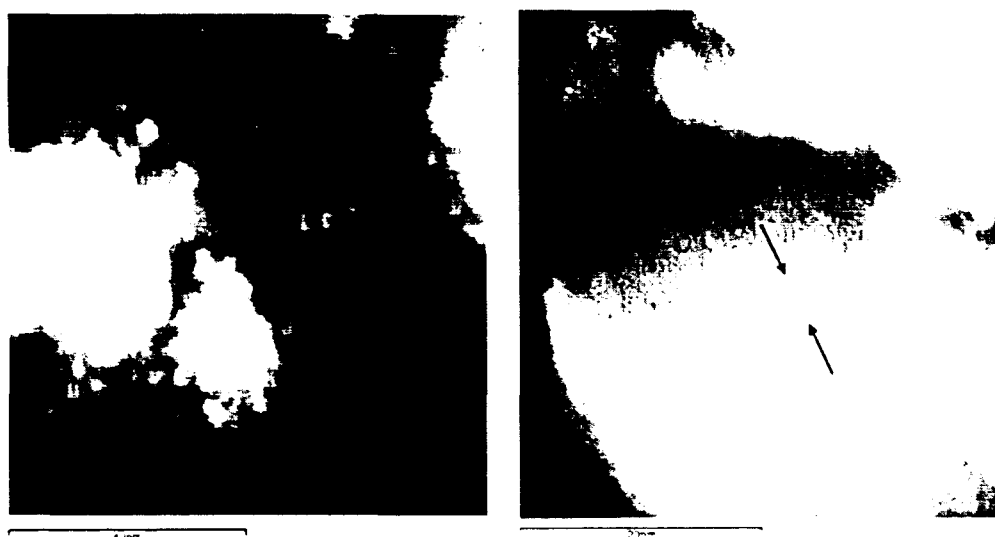


Figure 35 - HAADF images showing small Au-Pd alloy particles in 2.5at.%Au - 2.5at.%Pd TiO₂ (APT3). 800kX (left) and 1 MX (right)

Also, particle sizes in the pure gold and pure palladium systems are similar to those observed in the bi-metallic catalysts. This clearly indicates a synergistic promotion of the catalytic activity by gold and palladium alloying, rather than a morphological change being responsible for the increased $H_2O_2$ production.

It has further been reported that the impregnation process does not produce a very strong bond between metal particle and the oxide support [7]. The presence of such large Au-Pd particles in these catalysts may be a result of this poor bonding. If the atomic mobilities of the gold and palladium were sufficient, then the atoms would be able to agglomerate and grow over time, producing ever larger Au-Pd particles. This aspect of the bi-metallic catalysts made by impregnation brings into question their viability over time. However this aspect requires further study to determine whether the large particles are forming over time or whether they are an inherent by-product of the impregnation process.

Besides the types of particles discussed and shown above, a minority of the particles consisted of either pure gold (uncalcined $TiO_2$ sample only) or pure palladium (in the $TiO_2$ and $Al_2O_3$). Also, some particles observed formed alloy nanorods (observed in the calcined $TiO_2$ system only). An example of the first behavior is shown below in Figure 36. It is clear from the XEDS maps that there are particles which produce a palladium signal but no gold signal.

Similarly, Figure 37 below shows a faceted alloy nanorod structure in the $TiO_2$ system. It should be noted that maps presented in figures 36 and 37 were not subjected to MSA analysis.

**Figure 36** - HAADF image (top) of 2.5%Au-2.5%Pd/Al₂O₃ sample and corresponding XEDS maps of Pd (bottom left) and Au (bottom right), [100kX]

Also, Figure 38 shows a HAADF image and the corresponding XEDS

maps for the 2.5%Au-2.5%Pd/TiO₂ uncalcined sample. Clearly, there are gold particles

present which show no palladium. While the opposite was often seen in the calcined

TiO₂ and Al₂O₃ samples, pure gold particles were only observed in the uncalcined TiO₂

sample. Also present in these images are a few palladium particles that contain no gold,

and a larger particle which contains both. This data suggests that the compositional

nature of the metal particles in these catalysts is dependent on the heat treatment process

used. It is also interesting to note that the largest particle is approximately 80 nm in size,

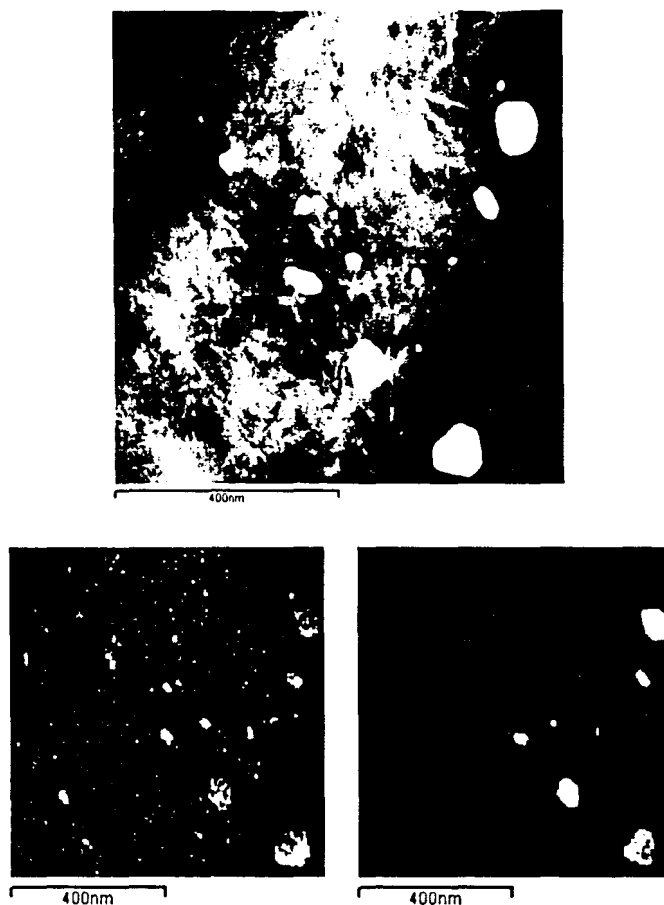suggesting that the large particles seen in all of the samples could be a by-product of the

**Figure 36** - HAADF image (top) of 2.5%Au-2.5%Pd/Al$_2$O$_3$ sample and corresponding XEDS maps of Pd (bottom left) and Au (bottom right), [100kX]

Also, Figure 38 shows a HAADF image and the corresponding XEDS maps for the 2.5%Au-2.5%Pd/TiO$_2$ uncalcined sample. Clearly, there are gold particles present which show no palladium. While the opposite was often seen in the calcined TiO$_2$ and Al$_2$O$_3$ samples, pure gold particles were only observed in the uncalcined TiO$_2$ sample. Also present in these images are a few palladium particles that contain no gold, and a larger particle which contains both. This data suggests that the compositional nature of the metal particles in these catalysts is dependent on the heat treatment process used. It is also interesting to note that the largest particle is approximately 80 nm in size, suggesting that the large particles seen in all of the samples could be a by-product of the
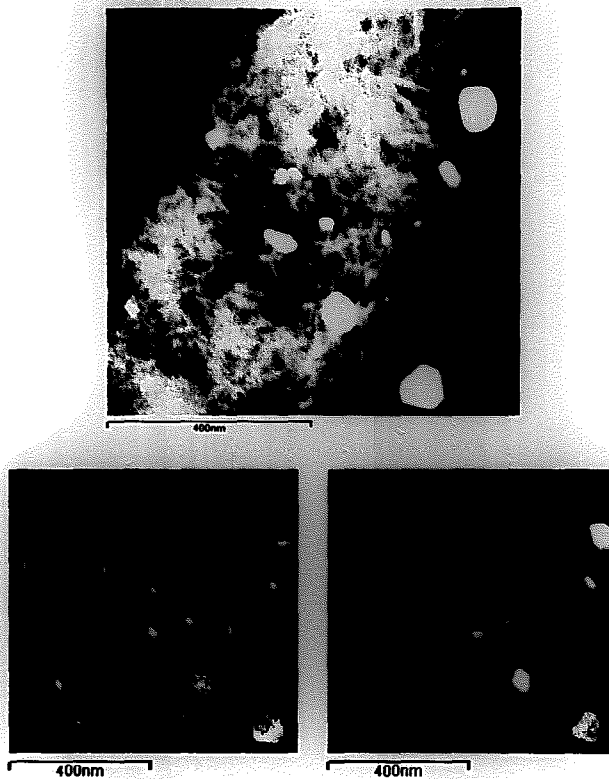
impregnation synthesis process, and not simply brought about by the calcination treatment.



Figure 37 - HAADF image (top left) of 2.5%Au-2.5%Pd/TiO₂ sample and corresponding XEDS maps of Au (top right), Pd (bottom left), and Ti (bottom right), [100 kX]

Since the $TiO_2$ catalysts showed the greatest activity of all the supports, it is important to consider the fact that these various morphologies and compositions are all observed to co-exist in the $TiO_2$ catalysts. However, nanorods and pure gold particles were not observed on either of the other supports.

Finally, the presence of NaCl particles was also detected by MSA analysis as shown below in Figure 39. By combining the Na and Cl signals it becomes clear that the two elements form a compound rather than existing separately. Presumably, the chlorine is derived from the gold precursor solution, aurochloric acid, as it was the only chlorine-

impregnation synthesis process, and not simply brought about by the calcination treatment.
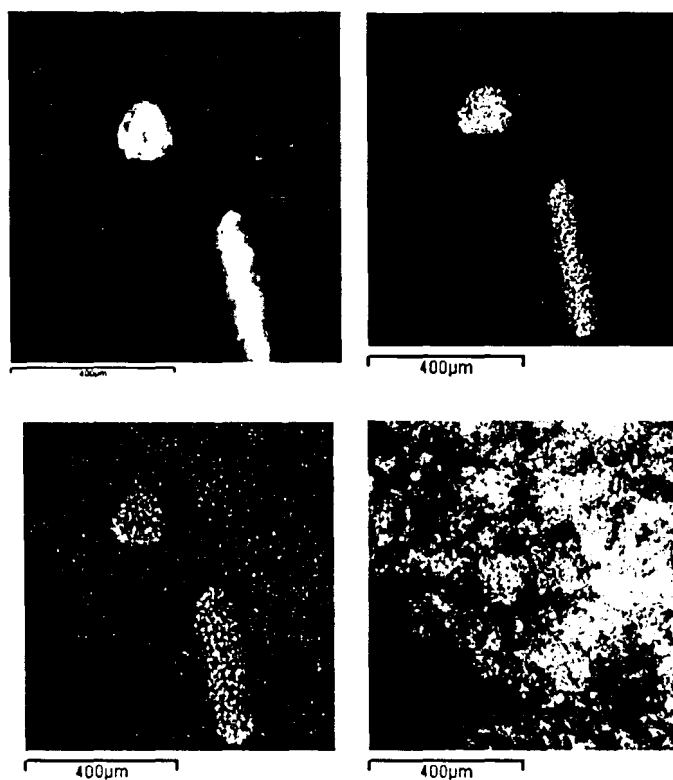


**Figure 37** - HAADF image (top left) of 2.5%Au-2.5%Pd/$TiO_2$ sample and corresponding XEDS maps of Au (top right), Pd (bottom left), and Ti (bottom right), [100 kX]

Since the $TiO_2$ catalysts showed the greatest activity of all the supports, it is important to consider the fact that these various morphologies and compositions are all observed to co-exist in the $TiO_2$ catalysts. However, nanorods and pure gold particles were not observed on either of the other supports.

Finally, the presence of NaCl particles was also detected by MSA analysis as shown below in Figure 39. By combining the Na and Cl signals it becomes clear that the two elements form a compound rather than existing separately. Presumably, the chlorine is derived from the gold precursor solution, aurochloric acid, as it was the only chlorine-

80

based component of the catalysts synthesis process. Similarly, the sodium most likely

comes from the $Na_2CO_3$ used to induce precipitation of the gold and palladium.



Figure 38 – HAADF image (top) of 2.5%Au-2.5%Pd/TiO$_2$ uncalcined sample and corresponding XEDS maps of Pd (bottom left) and Au (bottom right). [200kX]

While this type of image analysis was only performed on the iron oxide supported

catalysts, it would not be surprising to find NaCl particles in the other supports as well

since the synthesis process was rather similar in each case.

based component of the catalysts synthesis process. Similarly, the sodium most likely comes from the $Na_2CO_3$ used to induce precipitation of the gold and palladium.
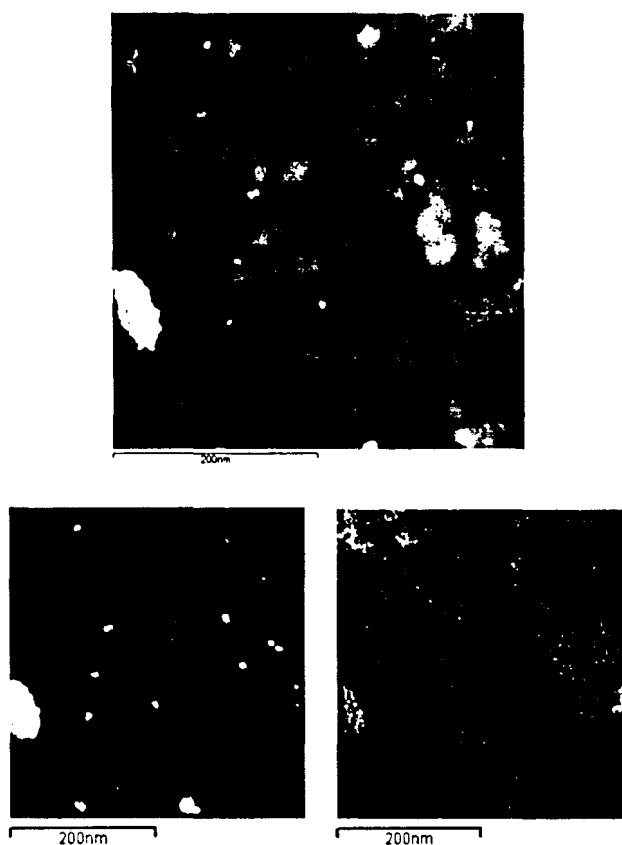


**Figure 38** – HAADF image (top) of 2.5%Au-2.5%Pd/TiO$_2$ uncalcined sample and corresponding XEDS maps of Pd (bottom left) and Au (bottom right), [200kX]

While this type of image analysis was only performed on the iron oxide supported catalysts, it would not be surprising to find NaCl particles in the other supports as well since the synthesis process was rather similar in each case.

**Figure 39** - HAADF image (left) of 2.5%Au-2.5%Pd/Fe$_2$O$_3$ and corresponding combined XEDS map (right) of Na and Cl signals; [100 µs dwell time]

### 3.4.4 Summary of Results of Au-Pd Bi-metallic Catalysts for H$_2$O$_2$ Production

In summary, adding gold to oxide supported palladium catalysts increases their activity for the hydrogen peroxide direct combination reaction regardless of the support material chosen, although the effect is most pronounced for the TiO$_2$ supports. The metal atoms in these catalysts prefer to form alloys, but instances have been observed where gold-only or palladium-only particles have formed. Since the particle sizes are not very dissimilar between the various catalysts, a synergistic altering of the palladium electronic structure in the particles seems to be responsible for their improved catalytic abilities.

TEM investigations have revealed a bimodal distribution of particles wherein there exist very large particles in excess of 30 – 70 nm in size as well as tiny particles that are less than 5 nm in size. The presence of particles this large is quite different from all the other catalyst systems investigated. It remains to be determined whether these particles form over time as a result of poor bonding of the metal particles to the oxide surface or if they are an inherent consequence of the impregnation process used to produce the catalysts.
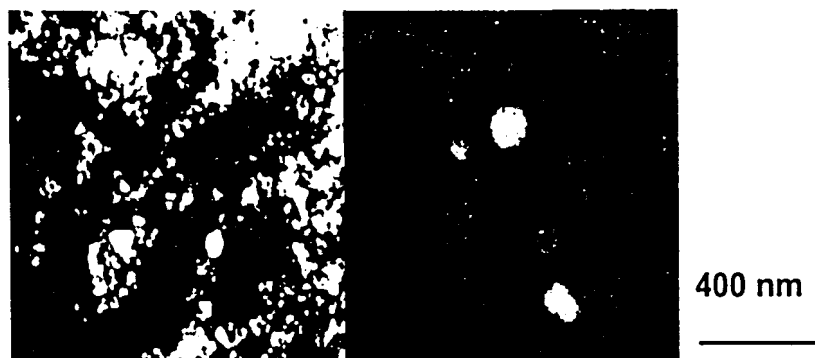
**Figure 39 -** HAADF image (left) of 2.5%Au-2.5%Pd/Fe$_2$O$_3$ and corresponding combined XEDS map (right) of Na and Cl signals; [100 μs dwell time]

### 3.4.4 Summary of Results of Au-Pd Bi-metallic Catalysts for H$_2$O$_2$ Production

In summary, adding gold to oxide supported palladium catalysts increases their activity for the hydrogen peroxide direct combination reaction regardless of the support material chosen, although the effect is most pronounced for the TiO$_2$ supports. The metal atoms in these catalysts prefer to form alloys, but instances have been observed where gold-only or palladium-only particles have formed. Since the particle sizes are not very dissimilar between the various catalysts, a synergistic altering of the palladium electronic structure in the particles seems to be responsible for their improved catalytic abilities.

TEM investigations have revealed a bimodal distribution of particles wherein there exist very large particles in excess of 30 – 70 nm in size as well as tiny particles that are less than 5 nm in size. The presence of particles this large is quite different from all the other catalyst systems investigated. It remains to be determined whether these particles form over time as a result of poor bonding of the metal particles to the oxide surface or if they are an inherent consequence of the impregnation process used to produce the catalysts.
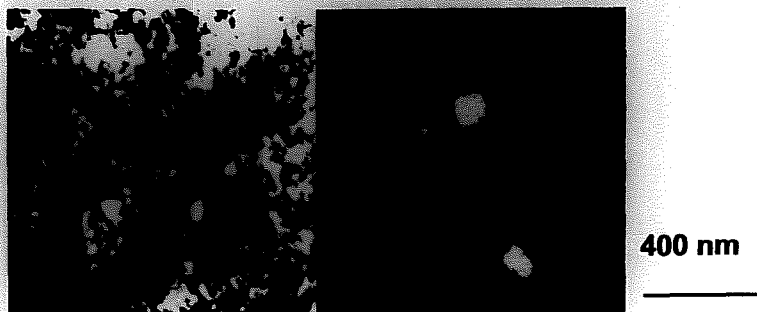
Several characterization techniques including XPS, HAADF-XEDS mapping, and HRTEM imaging suggest surface segregation of palladium, resulting in a core-shell particle structure. No oxide fringe patterns were evident in the lattice images suggesting that both the core and shell are metallic rather than oxidic in nature. It is hypothesized that the core-shell structure is a result of the preferential oxidation of palladium during the calcination process, which facilitates palladium migration to the surface. Subsequent reduction in $H_2$ converts the oxide to palladium metal, but the segregation is retained.

Particles of NaCl were also identified in the iron oxide support, and were identified as by-products of the impregnation process. It is presumed that similar particles may be present in the other supports as well, because the synthesis procedure was identical except for the support oxide used. Their role in promoting the reaction, if any, is unknown at this point.

# Chapter 4 – Conclusions and Suggestions for Future Work

The subtleties that exist between the various catalyst systems and reactions studied in this investigation make it difficult to come to any broad, general conclusions. What can be stated conclusively, no matter which system or reaction is considered, is that nearly every variable in the preparation process affects the performance of the resulting catalysts. These include, but are not limited to, the synthesis technique used, oxide support chosen, nominal gold content, calcination time, calcination temperature, and atmospheric conditions used during heat treatment. However, to be more specific requires a more delicate and systematic approach, so that what follows are conclusions reached separately for each catalyst examined.

## 4.1 Conclusions for Au/Iron Oxide for Low-temperature CO Oxidation

Contrary to observations reported for other oxide supports such as titania, calcination at elevated temperature is deleterious to the catalytic performance of Au/Iron oxide. Instead, a low-temperature drying process carried out in air produced a much more active catalyst. Even drying overnight at room temperature produced a remarkably active catalyst, while drying at 120 °C tended to maximize the activity for CO oxidation.

The reasons for this must relate to the electronic state of the gold particles present in the samples. The dried samples tended to consist mostly of cationic $Au^I$ with a metallic $Au^0$ minority, while the calcined samples showed the opposite character. This is due to the reduction of cationic gold to metallic gold that occurs at elevated temperatures. This disparity remained constant throughout the reaction.

There was also a definite correlation observed between the binding energy of the Au(4d) electron and catalytic activity in that a larger binding energy tended to produce a more active catalyst.

Gold particle size also played a major role in the catalytic activity observed. Particles of 2-4 nm in size were present in most of the dried samples while they were slightly larger, 5-8 nm, in the calcined samples. However, in three of the dried samples that exhibited high activity, no gold particles were resolved at all. This points to a possible role played by individual gold atoms or clusters of a few gold atoms that were beyond the imaging resolution of the instruments used. The correlation between particle size and gold oxidation states is not surprising, due to the metal-insulator transition undergone by metals at the nanoscale.

The oxide supports in the calcined samples consisted of large, well crystallized haematite particles. In contrast, the supports in the dried samples showed a mixture of very small haematite particles and layered regions, which may be indicative of the oxy-hydroxide goethite. This layered morphology was not observed in any of the sample calcined at 200 °C or above.

In the future, much work remains to done for the Au/Iron oxide system. Further identification of the role that the oxide support plays in the reaction is required. In particular, positive identification of the observed layered regions as goethite must be accomplished. This may be possible by high-resolution lattice imaging of the individual particles. By orienting the particle relative to the beam so that it is at a zone-axis and performing a Fourier Transform of the image would produce a pseudo-diffraction pattern.

The points in this pattern could be indexed and compared to the zone axes of goethite for positive confirmation.

Also, further investigation of the active gold site is necessary to determine whether or not there are single gold atoms or clusters taking part in the reaction. Due to the nature of such particles, they cannot be directly observed using conventional TEM or STEM techniques. However, recent improvements to electronic lens systems now allow for correction of the spherical aberration that significantly broadens the STEM beam and degrades the resolution of the instrument. Figure 25 shows an example of single atoms on an oxide surface that were resolved via aberration corrected STEM techniques. This major improvement to the instrumentation could play a significant role in settling the debate over whether 3.5 nm Au particles are the most active or whether much smaller particles are actually the dominant active site.


## 4.2 Conclusions for Au/Iron Oxide for Selective CO Oxidation in the Presence of $H_2$

Similar structural observations to the samples in the previous section were made for catalysts in this portion of the investigation. It was determined that samples that were highly active for CO oxidation also tended to promote the oxidation of $H_2$. In order to create a more CO selective catalyst, it was necessary to reduce the activity by means of a calcination treatment at elevated temperature. Above 400 °C, the selectivity to CO oxidation reaches 100 %. However, calcination at higher temperatures significantly reduced the CO oxidation activity, which reaches zero at 600 °C. Therefore, a calcination at 400 °C maximizes the selectivity while retaining excellent CO conversions.

## 4.3 Conclusions for Au/Zinc Oxide Catalysts for Methane Oxidation

An inverse relation between catalytic activity and ZnO particle size was observed. The addition of 1% Au reduced the ZnO particle size and increased the activity. Similarly, the addition of 2% Au further reduced the particle size and further increased the activity, but the addition of 5% gold caused the particle size to increase and activity to decrease.

It is hypothesized that the addition of highly dispersed (but not visible) gold therefore somehow inhibits the sintering of the ZnO, which increases the catalytic activity, but the reason that the addition of 5% Au reverses this trend is not well understood. Clustering of the dispersed atoms in the 5% sample may explain this observation but more analysis will be necessary to determine this.

Aberration corrected microscopy may be able to explain the mechanism by which adding gold seems to inhibit growth of the ZnO particles investigated for methane oxidation. As already discussed, single lanthanum atoms are known to have a similar inhibiting effect on the growth of alumina particles. However, only through aberration corrected imaging will it be possible to determine if this is also occurring in the ZnO catalysts.

## 4.4 Conclusions for the Bi-Metallic Catalysts for H₂O₂ Production

Adding gold to oxide supported palladium catalysts increases their activity for the production of hydrogen peroxide by direct combination of oxygen and hydrogen reaction regardless of the support material chosen, although the effect is most pronounced for the

TiO₂ supports. The metal atoms in these catalysts prefer to form alloys, but instances have been observed where gold-only or palladium-only particles have formed.

Impregnation produces a bimodal distribution of particles wherein there exist very large particles in excess of 30 – 70 nm in size as well as tiny particles that are less than 5 nm in size. In addition, alloy nanorods were observed in the $TiO_2$ system.

Palladium surface segregation was observed in the larger alloy particles, resulting in a Pd-rich shell surrounding a Au-rich core, both of which appear to be metallic in nature. The segregation is proposed to be brought about by the preferential oxidation of palladium during the calcination process, which induces palladium migration to the surface.

Particles of NaCl were also identified in the iron oxide support, and were identified as by-products of the impregnation process. It is presumed that similar particles may be present in the other supports as well, because the synthesis procedure was identical except for the support oxide used. The role of halide elements in promoting the reaction, if any, is unknown at this point.

Further investigation into the role played by the various types of metal particles in the catalysis of the reaction is necessary. The presence of very small and very large alloy particles, as well as separate, pure particles of gold and palladium and alternate morphologies such as nanorods makes these catalysts much more complicated than the other systems examined. In-situ EXAFS and XANES studies may be helpful in determining which of these particles adsorb the gas molecules and take part in the reaction.

Also, an examination of the structural interface between the various metal particles and the oxide supports should be carried out in an attempt to determine why titania supported catalysts are so much more efficient than alumina and haematite. HRTEM lattice imaging may shed some light on the shape and orientation of these particles relative to each other.

Next, an investigation into the particle size dependence of the composition of the alloy particles should be undertaken. It is possible that a variety of compositions exist and that it is highly dependent on the size of the particle in question.

In addition, a time related study of the very large metal particles should be carried out. The presence of such large particles raises the question of whether or not they are formed during the catalyst synthesis, or, rather, if they grow over an extended period of time. Only by observing newly made catalysts and observing any change in particle size over time will it be possible to determine this.

Finally, the core-shell structure identified in the present investigation must be more fully characterized. XEDS analysis using an aberration corrected beam may sufficiently increase the spatial resolution of this technique to permit accurate mapping of the smallest particles observed in the catalysts. This will allow a more convincing conclusion about the nature of the small particles to be reached in regards to whether they are pure gold and palladium or if they are in fact alloyed.

Also, improvements to spatial resolution may permit the more accurate determination of the thickness of the palladium shell as well as more accurate compositional analysis to determine the extent of segregation present. For example, it

may be possible to determine whether the shell consists entirely of palladium and the core

entirely of gold, or whether there is a less drastic compositional gradient between the two

# References

1. M. Haruta, T. Kobayashi, H. Sano, N. Yamada, *Chem. Lett.* 1987, 405.

2. T. Hayashi, K. Tanaka, M. Haruta, *J. Catal.* 1998, **178,** 566.

3. D. Andreeva, *Gold Bulletin* 2002, **35,** 82.

4. Z. Xu, F. S. Xiao, S. K. Purnell, O. Alexeev, S. Kawi, S. E. Deutsch, *Nature* 1994, **372,** 346.

5. M. Haruta, et al., *Catalysis Today*, 1997, **36,** 153.

6. M. Valden, X. Lai, D. W. Goodman, *Science*, 1998, **281,** 1647.

7. C. P. Poole Jr. and F. J. Owens, *Introduction to Nanotechnology*, Wiley, Hoboken, NJ, 2003.

8. J. H. Simmons and K. S. Potter, *Optical Materials*, Academic Press, San Diego, CA, 2000.

9. J. P. Borel et al., *Surface Science*, 1981, **106,** 1.

10. M. A. Bollinger and M. A. Vannice, *Appli. Catal. B: Environmental*, 1996, **8,** 417.

11. A. I. Kozlov, A. P. Kozlova, H. Liu and Y. Iwasawa, *Appli. Catal. A, Gen.* 1999 **182,** 9.

12. B. E. Nieuwenhuys, et al., *Catal. Lett.*, 1998, **56,** 195.

13. G. C. Bond and D. T. Thompson, *Gold Bulletin*, 2000, **33,** 41.

14. N. A. Hodge, C. J. Kiely, R. Whyman, M. R. H. Siddiqui, G. J. Hutchings, Q. A. Pankhurst, F. E. Wagner, R. R. Rajaram, S. E. Golunski, *Catalysis Today*, 2002, **72,** 133.

15. E. D. Park and I. S. Lee, *J. Catal.*, 1999, **186,** 1.

16. B. Qiao and Y. Deng, *Chem. Comm.*, 2003, 2192.

17. Q. Fu; H. Saltsburg; and M. Flytzani-Stephanopoulos, *Science*, 2003, **301,** 935.

18. J. W. M. H. Geerts, J. H. B. J. Hoebink, and K. V. D. Wiele, *Catal. Today*, 1990, 6, 613

19. J. Nakamara et al., *Catalysis Today*, 1996, 28, 223.

20. H. Sakurai and M. Haruta *Catalysis Today*, 1996, 29, 321.

21. P. Landon, P. Collier, A. J. Papworth, C. J. Kiely, and G. J. Hutchings, *Chem. Comm.*, 2002, 2058.

22. P. Landon, P. Collier, A. F. Carley, D. Chadwick, A. J. Papworth, A. Burrows, C. J. Kiely, and G. J. Hutchings, *Phys. Chem. Chem. Phys*, 2003, 5, 1917.

23. D. B. Williams and C. B. Carter, *Transmission Electron Microscopy*, Plenum Publ. Co., New York, 1996.

24. C. Boudais and D. Monceau, Carine Crystallography v. 3.1, Divergent Software, France, 1998.

25. C. Meyer and D. Hague, Digital Micrograph v. 3.6.5, Gatan Inc., 1999.

26. Inca Microanalysis Suite v. 4.04, Oxford Instruments, 1998.

27. M. Watanabe, Application of Principal Component Analysis on Spectrum-Imaging by X-Ray Energy Dispersive Spectrometry (personal communication / preparing)

28. J. C. Vedrine and B. Imelik, *Catalysts Characterization. Physical Techniques for Solid Materials*, Plenum Publ. Co., New York, 1994.

29. J. H. Scofield, Theoretical Photoionization Cross Sections from 1 to 1500 keV, Lawrence Livermore Laboratory Report UCRL-51326, 1973.

30. S. Eliot, *The Physics and Chemistry of Solids*, Wiley, West Sussex, England 2000.

31. J. Guzman and B. Gates, *J. of the Amer. Chem. Soc.*, 2004, 126, 2673.

32. Fisher Scientific Inc., Material Safety Data Sheet – Iron (III) Oxide, https://fscimage.fishersci.com/msds/11521.htm, 2003

33. V. Barron, et al., *American Mineralogist*, 1997, 82, 1091.

34. A. Gualtieri and P. Venurelli, *American Mineralogist*, 1999, 84, 895.

35. B. Grigorova, J. Mellor, A. Palazov, and F. Greyling, *WO Pat.*, 00 59631, 2000.

36. P. Porta, S. De Rossi, G. Ferraris, M. Lo Jacono, G. Minelli and G. Moretti, *Journal of Catalysis*, 1988, **109**, 367

37. G. Y. Wang, W. X. Zhang, H. L. Lian, D. Z. Jiang, and T. H. Wu, *Appl. Catal. A: General*, 2003, **239**, 1.

38. S. Wang, A. Y. Borisevich, S. N. Rashkeev, M. V. Glazoff, K. Sohlberg, S. J. Pennycook, and S. T. Pantelides, *Nature*, 2004, **3**, 143.

39. H. Okamato, et al., *Binary Alloy Phase Diagrams*, ASM International, OH, 1992.

40. L. Hilaire, P. Legare, Y. Holl, and G. Maire, *Surface Science*, 1981, **103**, 125.

41. P. Weinberger, L. Szunyogh, and B. I. Bennett, *Phys. Rev. B*, 1993, **47**, 154.

42. N. Bonnet, *Journal of Microscopy*, 1998, **190**, 2.

43. M. Watanabe et al., *Microscopy and Microanalysis Conference Proceedings*, to be published, 2004.

# Appendix A

## Collected XPS and EXAFS Data for Au/Iron Oxide Catalyst for Low Temperature CO Oxidation

### Table AI - XPS Binding Energy Differences (eV) for Au/Iron Oxide Catalysts

| Sample | Au(4d)-C(1s) | Au(4d)-Fe(2p) | Au(4d)-O(1s) | CO Conversion % |
|--------|--------------|---------------|--------------|-----------------|
| 12 | 50.3 | -375.8 | -193.5 | 66 |
| 12.1 | 51.7 | -376.3 | -194.5 | 32 |
| 12.2 | 51.4 | -375.7 | -194.3 | 65 |
| 12.3 | 50.4 | -376.9 | -195.2 | 7 |
| 12.4 | 50.1 | -376.2 | -195.2 | 26 |
| 14.1 | 49.7 | -376.4 | -195.6 | 0 |
| 14.2 | 51.7 | -375 | -193.5 | 100 |
| 15.1 | 50.93333 | -375.9 | -194.6 | 94 |

### TABLE AII: EXAFS Fit Parameters Characterizing $Fe_2O_3$-Supported Gold Samples Before Catalysis.[a]

| Backscatterer | dried sample | | | | calcined sample | | | |
|---|---|---|---|---|---|---|---|---|
| | $N$ | $R$ (Å) | $10^3 \times \Delta\sigma^2$ (Å$^2$) | $\Delta E_0$ (eV) | $N$ | $R$ (Å) | $10^3 \times \Delta\sigma^2$ (Å$^2$) | $\Delta E_0$ (eV) |
| Au–Au 1$^{st}$ shell | 8.3 | 2.79 | 9.12 | 1.91 | 10.7 | 2.85 | 10.18 | 1.77 |
| Au–Au 2$^{nd}$ shell | 4.1 | 3.89 | 8.34 | 7.27 | 6.2 | 3.99 | 11.12 | 6.03 |
| Au–O$_s$ | 1.4 | 2.04 | 1.49 | 5.51 | 0.9 | 2.10 | 4.13 | 8.73 |
| Au–O$_l$ | 1.3 | 2.59 | 0.24 | 1.02 | 0.4 | 2.64 | 6.31 | -2.63 |

[a] Notation: $N$, coordination number; $R$, distance between absorber and backscatterer atoms; $\Delta\sigma^2$, Debye–Waller factor; $\Delta E_0$, inner potential correction. Expected errors $N$: $\pm 10\%$, $R$: $\pm 0.02$ Å, $\Delta\sigma^2$: $\pm 20\%$, $\Delta E_0$: $\pm 20\%$. The subscripts s and l refer to short and long, respectively

# Appendix B
## Theoretical and Experimental Diffraction Data for Structural Identification

| Table BI - Theoretical and Experimental Ring Radius Ratios for Structural Determination of | | | |
|---|---|---|---|
| Au/Iron Oxide Catalysts via Electron Diffraction | | | |
| Calcined Sample Experimental Ratios | Dried Sample Experimental Ratios | Haematite Predicted XRD Ratios | Reflection |
| 1.00 | 1.00 | 1.00 | $Fe_2O_3$  1 0 -2 |
| 1.10 | - | - | Au      1 1 1 |
| 1.24 | - | - | Au      2 0 0 |
| 1.38 | 1.41 | 1.38 | $Fe_2O_3$  1 0 4 |
| 1.50 | 1.47 | 1.49 | $Fe_2O_3$  2 -1 0 |
| 1.62 | 1.64 | 1.65 | $Fe_2O_3$  0 0 6 |
| 1.86 | 1.86 | 1.85 | $Fe_2O_3$  2 0 2 |
| 2.10 | 2.18 | 2.12 | $Fe_2O_3$  2 0 -4 |
| 2.51 | 2.50 | 2.51 | $Fe_2O_3$  3 -1 -2 |

| Table BII - Theoretical and Experimental Ring Radius Ratios for Structural Determination of | | | |
|---|---|---|---|
| Au/Zinc Oxide Catalysts via Electron Diffraction | | | |
| Calcined Sample Experimental Ratios | Dried Sample Experimental Ratios | ZnO Predicted XRD Ratios | Reflection |
| 1.00 | 1.00 | 1.00 | ZnO  1 0 0 |
| 1.07 | 1.07 | 1.09 | ZnO  0 0 2 |
| 1.13 | 1.13 | 1.15 | ZnO 1 0 1 |
| 1.49 | 1.48 | 1.52 | ZnO  1 0 2 |
| 1.88 | 1.89 | 1.87 | ZnO  2 -1 0 |

# For Complete Pd Segregation
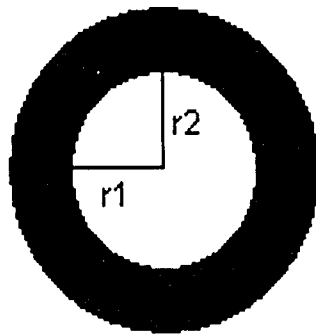


$$(4/3)\eth r_1^3 = (4/3)\,\eth(\,r_2^3 - r_1^3\,)$$
$$r_2 = 1.3 * r_1$$

Example: For 40 nm core, shell is only 12 nm thick

## Vita

Andrew Anthony Herzing was born in Ridgway, Pennsylvania on August $1^{st}$,
1980, the son of David Anthony Herzing and Cynthia Anne Herzing. After
graduating from Ridgway Area High School in 1998, he attended Lehigh University
in Bethlehem, Pennsylvania. During the summer of 2001, he worked as an intern at
IBM Microelectronics Inc. in East Fishkill, New York. He graduated with honors
from Lehigh University in 2002 with the degree of Bachelor of Science in Materials
Science and Engineering. In September of 2002, he began work towards this thesis in
the Materials Science and Engineering department at Lehigh University under the
supervision of Dr. Christopher Kiely.

# END OF TITLE